AGU PUBLICATIONS

JGR

Journal of Geophysical Research: Atmospheres

RESEARCH ARTICLE
10.1002/2015JD024711

Elevated aerosol layers and their radiative impact over Kanpur during monsoon onset period

Chandan Sarangi[1], S. N. Tripathi[1], A. K. Mishra[2], A. Goel[1], and E. J. Welton[3]

[1]Department of Civil Engineering, Indian Institute of Technology, Kanpur, India, [2]Centre for Environmental Science and Engineering, Indian Institute of Technology, Kanpur, India, [3]NASA Goddard Space Flight Center, Greenbelt, Maryland, USA

Abstract Accurate information about aerosol vertical distribution is needed to reduce uncertainties in aerosol radiative forcing and its effect on atmospheric dynamics. The present study deals with synergistic analyses of aerosol vertical distribution and aerosol optical depth (AOD) with meteorological variables using multisatellite and ground-based remote sensors over Kanpur in central Indo-Gangetic Plain (IGP). Micro-Pulse Lidar Network-derived aerosol vertical extinction (σ) profiles are analyzed to quantify the interannual and daytime variations during monsoon onset period (May–June) for 2009–2011. The mean aerosol profile is broadly categorized into two layers viz., a surface layer (SL) extending up to 1.5 km (where σ decreased exponentially with height) and an elevated aerosol layer (EAL) extending between 1.5 and 5.5 km. The increase in total columnar aerosol loading is associated with relatively higher increase in contribution from EAL loading than that from SL. The mean contributions of EALs are about 60%, 51%, and 50% to total columnar AOD during 2009, 2010, and 2011, respectively. We observe distinct parabolic EALs during early morning and late evening but uniformly mixed EALs during midday. The interannual and daytime variations of EALs are mainly influenced by long-range transport and convective capacity of the local emissions, respectively. Radiative flux analysis shows that clear-sky incoming solar radiation at surface is reduced with increase in AOD, which indicates significant cooling at surface. Collocated analysis of atmospheric temperature and aerosol loading reveals that increase in AOD not only resulted in surface dimming but also reduced the temperature (~2–3°C) of lower troposphere (below 3 km altitude). Radiative transfer simulations indicate that the reduction of incoming solar radiation at surface is mainly due to increased absorption by EALs (with increase in total AOD). The observed cooling in lower troposphere in high aerosol loading scenario could be understood as a dynamical feedback of EAL-induced stratification of lower troposphere. Further, the observed radiative effect of EALs increases the stability of the lower troposphere, which could modulate the large-scale atmospheric dynamics during monsoon onset period. These findings encourage follow-up studies on the implication of EALs to the Indian summer monsoon dynamics using numerical models.

Key Points:
- Persistent elevated aerosol layers (EALs) are found during monsoon onset period
- Strong radiative cooling is observed below elevated aerosol layers
- EAL's induced lower atmospheric stability imparts negative feedback to rising surface parcels

Supporting Information:
- Supporting Information S1
- Supporting Information S2

Correspondence to:
S. N. Tripathi,
snt@iitk.ac.in

Citation:
Sarangi, C., S. N. Tripathi, A. K. Mishra, A. Goel, and E. J. Welton (2016), Elevated aerosol layers and their radiative impact over Kanpur during monsoon onset period, *J. Geophys. Res. Atmos.*, *121*, 7936–7957, doi:10.1002/2015JD024711.

Received 23 DEC 2015
Accepted 16 JUN 2016
Accepted article online 24 JUN 2016
Published online 12 JUL 2016

1. Introduction

Aerosols are tiny solid or liquid particles suspended in Earth's atmosphere, which play a major role in global and regional climate [*Ramanathan et al.*, 2005]. Incoming solar radiation can be dominantly scattered or absorbed depending on the relative concentration and type of aerosols [*Boucher et al.*, 2013]. This perturbs the atmospheric as well as surface energy balance and thereby affects the regional hydrological cycle [*Ramanathan et al.*, 2001]. Aerosol extinction coefficient (σ) is an optical estimate of attenuation of incoming solar radiation due to presence of aerosols. Extinction is the most frequently measured optical quantity, which is highly correlated ($R^2 = 0.4–0.8$) with aerosol mass and number concentration [*Ozkaynak et al.*, 1985]. Limited information of 3-D aerosol distribution induces large uncertainties in estimates of aerosol radiative effects and their impacts on regional/global climate [*Boucher et al.*, 2013].

Kanpur, located in central Indo-Gangetic Plain (IGP), is one of the largest industrial cities in India. IGP is known as the food basket of India, and its agricultural productivity is mainly dependent on monsoon rainfall. Many studies, using ground-based Aerosol Robotic Network (AERONET) measurements [*Kaskaoutis et al.*, 2012], as well as various satellite retrieved data sets, such as Moderate Resolution Imaging Spectroradiometer (MODIS) [*Kaskaoutis et al.*, 2011], Multiangle Imaging Spectroradiometer (MISR) [*Dey and Di Girolamo*, 2011], and Total Ozone Mapping Spectrometer (TOMS) data [*Lal et al.*, 2012], identified IGP as a major hot spot of increasing

atmospheric pollution, with premonsoon being peak aerosol loading period [*Bollasina et al.*, 2008]. Growing energy demands of increasing population and associated rapid urbanization are responsible for the background increase in anthropogenic pollution in this region [*Dey and Di Girolamo*, 2011]. At the same time, the premonsoonal AOD distribution over IGP is associated with deepening of the Indian thermal low over northwest IGP [*Kaskaoutis et al.*, 2014]. Modeling of dust transport suggests that dust is transported across the Indo-Gangetic Basin at ~700–850 hPa altitude and accumulates over Himalayan slopes during March–May [*Das et al.*, 2013]. Using multisatellite and ground-based observations, *Badarinath et al.* [2010] suggested that the long-range transport of desert dust aerosols is favored by strong winds, both along the surface and in the middle troposphere. A clear relation of transported dust loading with increase in columnar AOD and decrease in columnar Angstrom exponent is suggested during premonsoon season over IGP [*Dey et al.*, 2004; *Badarinath et al.*, 2010]. Consequently, significant aerosol radiative forcing is also found during dust-dominated premonsoon periods over the IGP [*Chinnam et al.*, 2006; *Kaskaoutis et al.*, 2013; *Pandithurai et al.*, 2008; *Sharma et al.*, 2012; *Kumar et al.*, 2015, and references therein]. Modeling studies over different sites in IGP reveal that transported dust loading can potentially warm the atmosphere by 35–75 W m^{-2} during dust events over Kanpur [*Chinnam et al.*, 2006; *Kumar et al.*, 2015], 111–123 W m^{-2} during May–June 2006 over Delhi [*Pandithurai et al.*, 2008], and between 40 and 80 W m^{-2} during April–June 2010 over Patiala [*Sharma et al.*, 2012]. *Kaskaoutis et al.* [2013] reported a significant increase in elevated aerosol layer, aerosol radiative forcing, and heating rates over Kanpur during premonsoonal severe aerosol loading cases (2001–2010).

Das et al. [2015] examined the dynamic impact of large aerosol forcing on the atmospheric temperature and circulation over India using a regional climate model and showed a positive feedback of aerosol radiative effect on summer monsoon circulation. General circulation model (GCM) results show that premonsoonal accumulation of aerosols over southern slopes of Himalayas can potentially alter the South Asian monsoon circulation [*Lau et al.*, 2006]. *Lau et al.* [2006] hypothesized that the presence of solar absorbing aerosols over the Himalayan slopes and region around the Tibetan Plateau can cause midatmospheric warming, which in turn enhances Hadley circulation during premonsoon period. These processes draw more warm and moist low-level inflow from Indian Ocean and eventually strengthen the monsoon. This hypothesis is termed as the Elevated Heat Pump (EHP) mechanism. *Kuhlmann and Quaas* [2010] contradicted the EHP hypothesis by simulating radiative forcing using observed premonsoonal vertical aerosol profiles from Cloud-Aerosol Lidar and Infrared Pathfinder Satellite Observations (CALIPSO). On a slightly contradictory note, the solar dimming theory claimed that decrease in surface radiation due to aerosol masking over India could lead to weakening of the meridional sea surface temperature gradient and the meridional overturning circulation eventually resulting in reduction of monsoonal rainfall [*Ramanathan and Carmichael*, 2008; *Bollasina et al.*, 2011, 2008; *Chung and Ramanathan*, 2006; *Cherian et al.*, 2013]. Therefore, improved understanding of aerosol vertical distribution and their physical and radiative properties is essential [*Kinne and Pueschel*, 2001; *Gadhavi and Jayaraman*, 2006], mainly during the monsoon onset period.

Mishra and Shibata [2012] reported the CALIPSO-retrieved monthly mean backscatter profiles for 2006–2009 over central IGP. They found elevated aerosols up to 4 km during mid-April to mid-June with maximum altitudes during May. Similar results are also reported by *Gautam et al.* [2009] during April–May 2008. Another recent study [*Misra et al.*, 2012] illustrates elevated aerosol layers (EALs) using ground-based lidar measurements over Kanpur during premonsoon. Modeled heating rate profiles during this period show peak heating rate at 2–4 km [*Jaidevi et al.*, 2011; *Gautam et al.*, 2009, 2010; *Kuhlmann and Quaas*, 2010]. However, quantitative characterization of the aerosol profile and perturbation to atmospheric stability due to EALs remained unexplored in those studies. Due to the temporal limitations of CALIPSO observations (one scan per daytime), previous studies [*Mishra and Shibata*, 2012; *Misra et al.*, 2012] also lack information on daytime variation of aerosol vertical distribution.

In this study, we use Micro-Pulse Lidar Network (MPLNET)-derived σ profiles during May–June for 2009, 2010, and 2011 to characterize and quantify the mean vertical distribution of aerosols, particularly EALs, over Kanpur. We have also examined the interannual and daytime variability of EALs during the study period. Cotemporal σ and radiosonde measurements are used to investigate the associations of meteorological parameters with daytime (morning versus evening) variation of EALs. Further, we investigated the radiative impact of EALs on incoming shortwave solar radiation using observations and radiative model simulations. Finally, the regional implication of EALs on observed atmospheric temperature and atmospheric stability is discussed. The present study shows the importance of radiative effect of EALs on atmospheric stability during

monsoon onset period, which could enable better understanding on aerosol's implications to summer monsoon dynamics over the IGP.

2. Materials and Methodology

2.1. Aerosol Measurements

The Micro-Pulse Lidar Network (MPLNET) is a global network of backscatter elastic lidar collocated with Aerosol Robotic Network (AERONET) [*Holben et al.*, 1998] Sun/sky photometer. We used level 2 columnar AOD (500 nm) and Angstrom exponent (440–675 nm) along with level 2 σ profiles (20 min temporal and 75 m vertical resolution), which are retrieved from AERONET and MPLNET, both located at Indian Institute of Technology-Kanpur (IITK). The following periods are analyzed in this study: (a) 15 May to 15 June (31 days) in 2009, hereafter referred to as P9; (b) 1 May to 15 June (46 days) in 2010, P10; and (c) 1 May to 15 June (46 days) in 2011, P11. MPLNET site became functional at Kanpur from 15 May 2009; hence, the period 1 May to 15 May in 2009 is not included in our study. AERONET-derived columnar AOD retrievals have an uncertainty of approximately $\pm$0.01 at 500 nm [*Eck et al.*, 1999].

MPLNET Level 0 data consists of near-real-time measured raw data (photon counts). The algorithm for converting these raw data (Level 0) to uncalibrated backscatter (Level 1) is described in *Campbell et al.* [2002]. Level 1 product provides combined profiles from molecular and aerosol backscatter at every 75 m from surface to 60 km. To separate molecular contribution from the total signal, the calibration process used constructed Rayleigh optical functions [*Welton et al.*, 2000]. To create aerosol extinction profiles (Level 1.5), Level 1 profiles are constrained by collocated aerosol optical depth (AOD) measurements (from AERONET Sun photometer) and a constant (throughout the column) columnar-averaged lidar ratio (extinction-to-backscatter ratio) is retrieved. These processed profiles are available at a frequency of 20 min. Moreover, Level 1.5 product may contain errors related to temperature of instrument and cloud contamination. Level 2 data, the final quality assured MPLNET product, is created by omitting these bad data from Level 1.5. Uncertainties in MPLNET instruments for raw signal and measured background are negligible (about 0.3%), but the uncertainty in energy monitoring due to fluctuations in incoming data rate is 1–5%. However, the highest uncertainty in measured backscatter is due to near-surface optical overlap. Details about calculations of these uncertainties and their correction terms are documented in *Welton and Campbell* [2002]. The lowest recoverable altitude is 400 m for newer MPL models due to instrumental error and near-surface retrieval error. The overall uncertainty in aerosol backscatter retrieval is 13×10^{-5} km^{-1} sr^{-1} at around 530 nm [*Misra et al.*, 2012]. As aerosol lidar ratio varies with altitude, the assumption of constant columnar lidar ratio can also contribute to uncertainties in Level 2 aerosol extinction profiles [*Welton et al.*, 2000].

We have also used Cloud Aerosol Lidar with Orthogonal Polarization (CALIOP) on board CALIPSO satellite retrieved aerosol profiles [*Winker et al.*, 2009]. We have used daytime/nighttime CALIOP Level 2 version 3.02 aerosol extinction (at 532 nm) product [*Young and Vaughan*, 2009] to support our analysis on interannual and diurnal variation of EALs. It should be noted that daytime profiles have possible noises due to solar interference. All aerosol profiles are screened for possible artifacts (cloud contamination) using a standard scheme given by *Winker et al.* [2013].

2.2. Meteorological Measurements

National Oceanic and Atmospheric Administration (NOAA) Air Resources Laboratory (ARL) Hybrid Single-Particle Lagrangian Integrated Trajectory (HYSPLIT) PC version model [*Draxler and Hess*, 1997] is used to calculate 7 days air mass backward trajectories at three altitudes (1.5, 2.5, and 3.5 km) at 1130 LT. Gridded (1° $\times$ 1°) wind fields from the Global Data Assimilation System (GDAS) [*Parrish and Derber*, 1992] are used as input. Hourly mixing layer height over Kanpur is also obtained from these HYSPLIT calculations.

Upper air radiosondes with 12-hourly temporal resolution (0530 and 1730 local time) for P9 at Indian Meteorological Department's (IMD) Lucknow station (26.5°N, 80.5°E) are used to understand the association of aerosol profile and meteorological variables. The 12-hourly resolved radiosonde measurements are not available during P10 and P11. This data set is available from the website of University of Wyoming (http://weather.uwyo.edu). Many previous studies have also used the radiosonde measurements from Lucknow and Delhi to represent the atmospheric stability and wind circulation conditions in the context of aerosol variability over the entire IGP [*Bhattacharjee et al.*, 2007; *Mishra and Shibata*, 2012]. Lucknow's IMD station (128 m above sea level) and IITK (123 m above sea level) are located only 60 km apart on a plain terrain. Moreover, temporal averaging (15 May to 15 June) of profiles will also suppress short time scale differences in

the atmospheric structure. Therefore, the mean thermodynamic structure of Lucknow could be representative of that over Kanpur.

Virtual potential temperature (VPT) is used as a stability criteria when vertical moisture gradient exists in the atmosphere. *Seidel et al.* [2010] showed that the uncertainty in determining the extent of boundary layer by this conservative method is a few hundred meters. A typical radiosonde profile provides measurements of meteorological variables such as horizontal wind speed, temperature (T), and mixing ratio (q). T and q are grouped and averaged in vertical bins of 500 m from 0.5 km to 6 km altitudes. These parameters are used in equation (1) as inputs to calculate corresponding VPT profiles [*Srivastava et al.*, 2011].

$$\mathrm{VPT} = (1 + 0.61 \times q) \times T \times (p_o/p)^k \tag{1}$$

where $k = R/C_p$, q is the moisture mixing ratio, p_o is surface pressure, C_p is specific heat at constant pressure, R is the gas constant, and T and P are temperature and pressure at the altitudes where VPT is computed. Mean VPT profiles during morning and evening periods of P9 are created by averaging all the VPT profiles available within these periods. Mean cotemporal VPT and σ profiles are used to examine the association between daytime variability of aerosol profiles and local atmospheric structure.

2.3. Solar Flux and Temperature Measurements

Measurements of total solar flux at surface available from a Kipp and Zonen CM 21 pyranometer established under the Solar Radiation Network (SolRad-Net) [*Schafer et al.*, 2002] are used to understand the aerosol-induced radiative extinction of incoming solar radiation. The pyranometer is collocated with the AERONET and the MPLNET at IITK. The pyranometer measures the instantaneous downwelling total solar flux (305–2800 nm) at surface (TS_{SRF}) every 2 s within an uncertainty of 2%. These instantaneous measurements are cloud screened by employing twofold prepossessing methodology. First, only temporally collocated instantaneous flux measurements with concurrent Level 2 AERONET measurements (cloud screened) within a ±5 min time frame are selected. Although this process assures the absence of cloud along the direct Sun beam path, the possible cloud effect on the diffuse component cannot be eliminated. The clouds close to the Sun's disc (which do not obscure the direct Sun beam) can also increase the total solar radiation at surface due to increased diffuse component [*Gu et al.*, 2001]. To avoid this effect from the scattered and peripheral clouds in the hemispherical field of view, a measurement is eliminated if its root-square-mean error within the ±30 min temporal running box is greater than 0.75% of that solar measurement. Similar data processing methodologies to remove sudden fluctuating measurements due to influence from scattered clouds have been used in previous studies [*Conant*, 2000; *Gautam et al.*, 2010; *RosáRio et al.*, 2011]. The magnitude of the clear-sky incoming shortwave flux at the surface at any given time is dependent on the thickness of the atmospheric layer crossed by the incident ray before reaching the surface, which varies with the solar zenith angle of the Sun. To remove the dependency of our clear-sky sampled fluxes on variability in solar zenith angle (SZA), observed cloud-screened solar fluxes are divided with cosine of solar zenith angle to create normalized solar fluxes at surface [*Long and Ackerman*, 2000]. Finally, our analysis is restricted to a narrow interval between 25° and 40° solar zenith angle (SZA) between 1200 and 1500 LT to focus our analysis on the attenuation of solar flux mainly due to aerosols [*Gautam et al.*, 2010].

The spaceborne Clouds and the Earth's Radiant Energy System (CERES)-observed top of the atmosphere (TOA) fluxes are used to estimate the impact of aerosol loading on outgoing radiation fluxes [*Wielicki et al.*, 1996]. CERES's 1-hourly (1° × 1°) gridded Single Scanner Footprint (SSF) data product considers MODIS-observed cloud and aerosol properties in estimating the outgoing shortwave (SW) radiation fluxes. The fluxes are obtained from measured radiances using angular distribution models [*Loeb and Kato*, 2002]. The error in SW_{TOA} due to the radiance to flux conversion has been estimated to be ~3%. We used SW_{TOA} (0.3–5μm) clear-sky SSF1deg-Ed4a flux and collocated MODIS-AOD products [*Platnick et al.*, 2003] available at AQUA overpass time (1330 LT) during our three study periods. We used linear regression between SZA normalized SW_{TOA} and collocated MODIS-AOD over the region 25–27°N and 79–81°E centered at IITK (26.3°N, 80.2°E) to get a statistically significant estimate of the TOA radiative forcing efficiency of aerosol loading. The MODIS-AOD has been extensively validated against AERONET measurement over Kanpur [*Tripathi et al.*, 2005a]. The expected uncertainty of MODIS-AOD is ± 0.05 ± 0.15 × AOD over land [*Remer et al.*, 2005]. Previous studies have also estimated the surface and TOA radiative forcing efficiency over IGP using CERES measurements [*Gautam et al.*, 2010, 2011].

We have also used 1° × 1° gridded columnar MODIS-derived aerosol optical depth (AOD at 550 nm) and the Atmospheric Infrared Sounder (AIRS)-derived temperature (1° × 1° spatial resolution) at five pressure levels over the region 25–27°N, 79–81°E to analyze the effect of EALs on atmospheric stability. Both MODIS and AIRS products (collection 6) are retrieved at Aqua overpass time (~1330 LT). The AIRS temperature data are sorted according to MODIS-AOD and divided into nine bins of 10% each. *Davidi et al.* [2009] and *Mishra et al.* [2014] have previously used this methodology to estimate aerosol-induced temperature perturbation over the Amazon and Mediterranean Basin, respectively. Validation of AIRS temperature against radiosonde measurements showed that the AIRS temperature measurements have an uncertainty of ~1 K/1 km atmospheric layer [*Aumann et al.*, 2003]. Details on accuracy and validation of AIRS temperature product are documented elsewhere [*Aumann et al.*, 2003; *Diao et al.*, 2013, and references therein].

Clear-sky SW (0.25–4μm) radiative transfer calculations are done using a columnar radiative transfer computer code known as Santa Barbara DISORT (discrete ordinates radiative transfer) Atmospheric Radiative Transfer Model (SBDART) [*Ricchiazzi et al.*, 1998]. Discrete ordinate method is used for numerical integration of the radiative transfer equations, which provides a numerically stable algorithm to solve the equations of plane-parallel radiative transfer in a vertically inhomogeneous atmosphere [*Stamnes et al.*, 1988]. This algorithm includes multiple scattering in a vertically inhomogeneous, nonisothermal plane-parallel media. Solar zenith angle, surface albedo, the spectral aerosol optical depth, the spectral single-scattering albedo, and the spectral asymmetry parameter are inputs required for characterization of the atmospheric aerosol radiative effects. Aerosol properties are provided from IITK AERONET measurements. The spectrally invariable surface albedo (0.22) over the region is provided using MODIS land product. The MPLNET-derived aerosol vertical extinction is also used as an input. AIRS-derived (over Kanpur) profiles of water vapor, ozone mixing ratio, and temperature are used for atmospheric model. Keeping all other inputs same, we performed four SBDART simulations with different aerosol profile scenarios (four equal AOD bins of 25% each) and one simulation without aerosols (AOD = 0). The atmospheric heating rate for each layer is calculated using equation (2) [*Liou*, 2002].

$$dT/dt = g/C_p \times \Delta F/\Delta P \tag{2}$$

where T is the temperature (K), t is the time (s), g is the gravitational acceleration (9.8 ms^{-2}), C_p is the specific heat of dry air (1004 J/kg/K), ΔF is the net SW flux (W m^{-2}), and ΔP is the pressure difference between the layers (Pa). The aerosol heating rate is calculated as the difference in heating rates between simulations with and without aerosols.

We have used data sets from several sources (ground based, satellite, and reanalysis) to provide an overall perspective of elevated aerosol layers over Kanpur. First, we have characterized and quantified the interannual and daytime variations in SLs and EALs using MPLNET-derived σ profiles. We have used measurements from collocated AERONET site to understand how EALs change with columnar aerosol properties. CALIPSO-derived aerosol profiles and HYSPLIT-calculated back trajectories are used to understand the interannual variability of EALs, while radiosonde measurements were used to investigate the association of atmospheric structure on daytime variation of EALs. In section 3.4, we have investigated the radiative impact of EALs. Cotemporal pyranometer-measured radiation flux and AERONET-AOD measurements along with collocated CERES-flux and MODIS-AOD data set are used to estimate the aerosol SW radiative forcing efficiency at surface, atmosphere, and TOA over Kanpur. SBDART radiative model simulations are used to investigate the role of EAL-radiation interactions in the observed radiative forcing of increasing aerosols. Finally, the collocated and cotemporal AIRS-temperature and MODIS-AOD data are used to understand the regional implication of EALs on observed atmospheric temperature and atmospheric stability. We note that various different data sets with different sampling frequency are used in this study. For any particular analysis, we have sampled the analyzed parameters at same time or within small time interval. It should be noted that the present limitation to the data availability and their frequency may affect the results in view of daytime variation. Therefore, this issue is highlighted while discussing the respective results (wherever applicable).

3. Results and Discussion

3.1. Mean Vertical Distribution of Aerosol and Its Interannual Variation

Seinfeld and Pandis [2006] have stated that generally, σ decreases exponentially under standard atmospheric structure with maximum σ near surface as represented in equation (3) below.

$$E(z) = E(\text{surf}) \times \exp(-z/h_{SL}) + F, \tag{3}$$

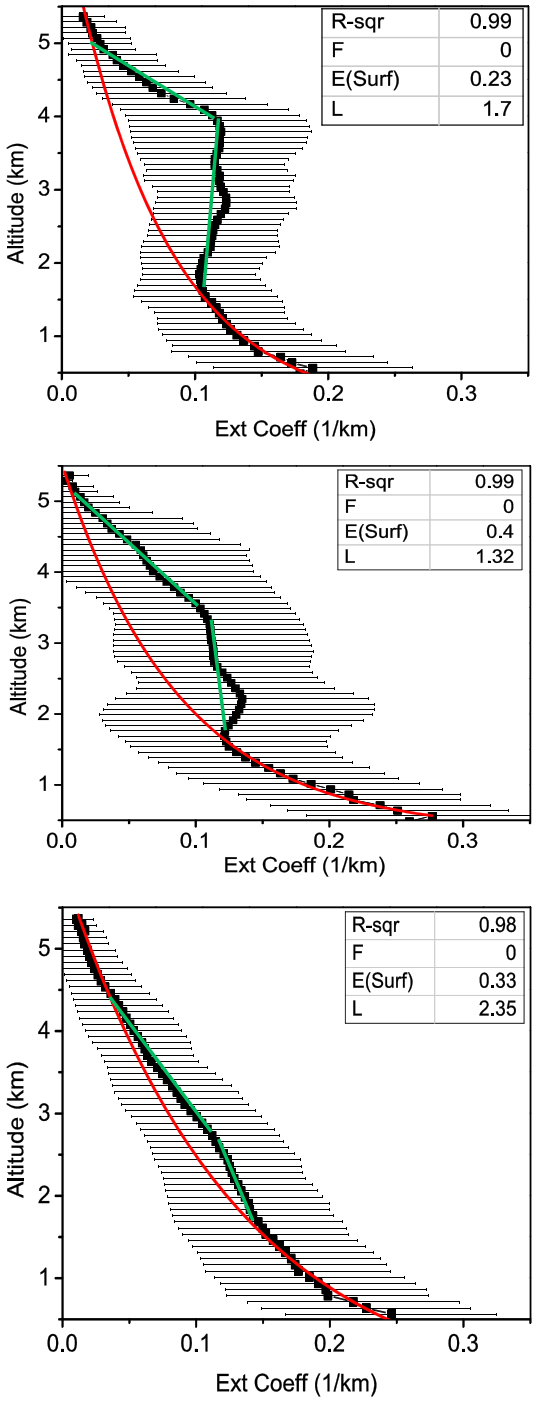

Figure 1. Mean σ profiles (black) with standard deviation during (top) P9, (middle) P10, and (bottom) P11. The red lines represents the exponential fit (equation (1)) to the mean σ values between 0.5 km and 1.5 km. The green lines show the aerosol gradient changes within EAL for each period. The legend box shows the modeled parameters for this fit (refer text for explanation). L is the fitted scale height (h_{SL}).

where $E(z)$ is extinction at altitude z, F is offset, E(surf) is the estimated extinction at surface, and h_{SL} is the scale height of mean σ profile of surface layer (SL) (SL will be explained below). Scale height (h_{SL}) indicates the height within which σ will be exponentially reduced by a factor of e.

Figure 1 shows the mean σ profiles during P9 (top), P10 (middle), and P11 (bottom) using the available MPLNET measurements. Extinction coefficient decreases exponentially with height from about 0.5 km to 1.5 km in all three periods. Equation (3) is fitted to average σ profile between 0.5 km and 1.5 km. These fitted curves have adjusted R^2 value of 0.99 during P9 and P10 and 0.98 during P11. They are extended to 6 km altitudes (red colored lines in Figure 1). The comparison of the theoretical fitted curve and the actual measured mean σ profile highlights the EAL over Kanpur. The aerosol gradient within the EALs is shown in green. The thin horizontal bars represent the standard deviation at discrete heights. The total number of profiles available in each period, scale height (h_{SL}), E(surf), and EAL_{crt} for the profiles is mentioned in Table 1.

We find that h_{SL}, E(surf), and EAL_{crt} are different during each period (Table 1). The scale height (h_{SL} = 2.35) in P11 is higher relative to that observed during P9 (1.70) and P10 (1.32), which implies slow rate of exponential decay in aerosol extinction during P11. Above 1.5 km (Figure 1) the change in vertical gradient of aerosol is relatively small up to a critical altitude (EAL_{crt}). Above EAL_{crt}, aerosol gradient decreases steeply with height and the σ value becomes very small above 5.5 km. The mean aerosol vertical structure over Kanpur during May–June period can be categorized into 2 layers: (a) surface layer (SL), surface to 1.5 km, where σ exponentially decreased with altitude, and (b) EAL, 1.5 km to 5.5 km where σ significantly diverges from the theoretical curve. We numerically calculate AOD using equation (4) to quantify the amount of aerosol present in SL and EAL.

$$\mathrm{AOD} = \int_{z1}^{z2} (\sigma)\mathrm{d}z \qquad (4)$$

where altitude $z1$ and $z2$ are 0 km (1.5 km) and 1.5 km (5.5 km) for SL (EAL), respectively. σ measurements are available at a constant vertical resolution of 75 m. We assume that σ remained constant within these 75 m vertical layer. Hence, dz is equal to the width of the layer in equation (4). Due to unreliable σ values below 0.5 km, we extrapolate the exponential fitted curves to get the σ values between 0 km and 0.5 km.

Table 1. This Table Illustrates Measured and Fitted Parameters of Mean Annual (Figure 1) and Daytime Segregated (Figure 4) Aerosol Profiles Used in This Study[a]

Period	No. of Profiles	h_{SL} (km)	E(Surf) (km^{-1})	AOD_{SL}	EAL_{crt} (km)	AOD_{EAL}	$FAOD_{EAL}$ (%)
P9	322	1.71	0.23	0.22	3.8	0.33	60.1
P10	225	1.32	0.4	0.33	3.4	0.33	50.1
P11	239	2.35	0.33	0.31	2.6	0.32	51.0
P9M	114	1.84	0.19	0.20	3.9	0.43	64.4
P9N	93	1.47	0.27	0.25	3.9	0.36	58.4
P9E	115	1.87	0.25	0.23	2.8	0.34	59.2
P10M	93	1.1	0.4	0.3	4.6	0.44	59.4
P10N	45	0.99	0.51	0.36	3.8	0.28	43.6
P10E	87	1.5	0.33	0.3	2.3	0.32	51.8
P11M	72	2.42	0.33	0.3	3.3	0.33	52.3
P11N	35	2.57	0.39	0.36	2.6	0.30	45.0
P11E	132	2.33	0.33	0.30	2.6	0.29	48.9

[a]The number of profiles used, scale height of SL (h_{SL}), estimated extinction at surface (E(surf)), mean AOD of surface layer (AOD_{SL}), EAL_{crt} (location of change in aerosol gradient within EAL), mean AOD of elevated aerosol layer (AOD_{EAL}), and fractional contribution of EAL to columnar AOD ($FAOD_{EAL}$) for each study period is reported in different columns. M, N, and E represent the morning, midday, and evening period of the three study periods, respectively.

Thus, the SL would be treated as aerosol layer between 0 and 1.5 km in further sections. The computed AOD for SL (AOD_{SL}) and EAL (AOD_{EAL}) and the fractional contribution from EAL to total columnar AOD ($FAOD_{EAL}$) for the mean profiles are estimated and reported in Table 1.

$FAOD_{EAL}$ is 0.60 ± 0.16, 0.50 ± 0.19, and 0.51 ± 0.08 in P9, P10, and P11, respectively. On an average, about 50% of aerosols are lifted to EAL, which indicates that EALs are a persistent feature during monsoon onset period over Kanpur. Figure 1 shows that the mean aerosol extinction coefficient varies from 0.05 to 0.1 km^{-1}, 0.01 to 0.12 km^{-1}, and 0.015 to 0.15 km^{-1} in EAL during P9, P10, and P11, respectively. The maximum σ in SL (500 m) is found to be 0.28 km^{-1} (in P10) followed by 0.25 km^{-1} (in P11) and 0.19 km^{-1} (in P9). The persistent EALs are also present in daily mean σ profiles for P9, P10, and P11 (Figure S1 in the supporting information). The shape of EALs has different feature during P11 as compared to P9 and P10. The lofted distinct parabolic shape of EALs present during P9 and P10 is flattened in P11. During P9 and P10, higher σ values are observed at altitude above 3 km compared to P11, but between 1 and 3 km, higher σ values are observed during P11. These interannual differences could be the result of variations in aerosol advection at different altitudes (discussed below) along with interannual variability of local atmospheric structure.

Similar types of mean aerosol profiles are reported by *Komppula et al.* [2012], who found aerosol extinction coefficients of 0.1–0.25 km^{-1} between 2 and 4 km altitudes using Raman lidar over Delhi during premonsoon season (2008–2009). *Mishra et al.* [2010] have found about 55% contribution from elevated aerosols (1–3.5 km) to total columnar AOD during June 2008 over west coast of peninsular India using Micro-Pulse Lidar (MPL). Another study over the eastern coast of India (Visakhapatnam) also shows dominance of elevated aerosol layer from 1.6 to 5.0 km during premonsoon 2006 [*Niranjan et al.*, 2007]. The study reported that the AOD of elevated aerosol layer could go as high as 0.25 in severe aerosol loading conditions [*Niranjan et al.*, 2007]. *Sinha et al.* [2013] have reported 25% contribution from elevated aerosol layer (above 3.5 km) over Hyderabad during premonsoon, 2009–2010. In another study using MPL, 40–60% contribution of aerosol above 1.0 km during March 2005 were reported over Bangalore [*Satheesh et al.*, 2006]. The comparison of our results with those of other studies indicates the persistent nature of EALs over India, which have notable spatiotemporal variability. However, the shape and σ values of EALs observed over IGP have significant differences compared to EALs over the southern part of India. Cloud Aerosol Interaction and Precipitation Enhancement Experiment (CAIPEEX) campaign (2009) measurements show almost two order higher aerosol mass concentrations in EALs over IGP than that over Southern India [*Kulkarni et al.*, 2012].

To visualize the association between EALs and columnar aerosol properties, we plot the columnar AOD (AOD_{col}) and Angstrom exponent from AERONET measurements as a function of MPLNET-derived $FAOD_{EAL}$ in Figure 2. We have divided all the collocated (AERONET-MPLNET) samples during P9, P10, and P11 period into

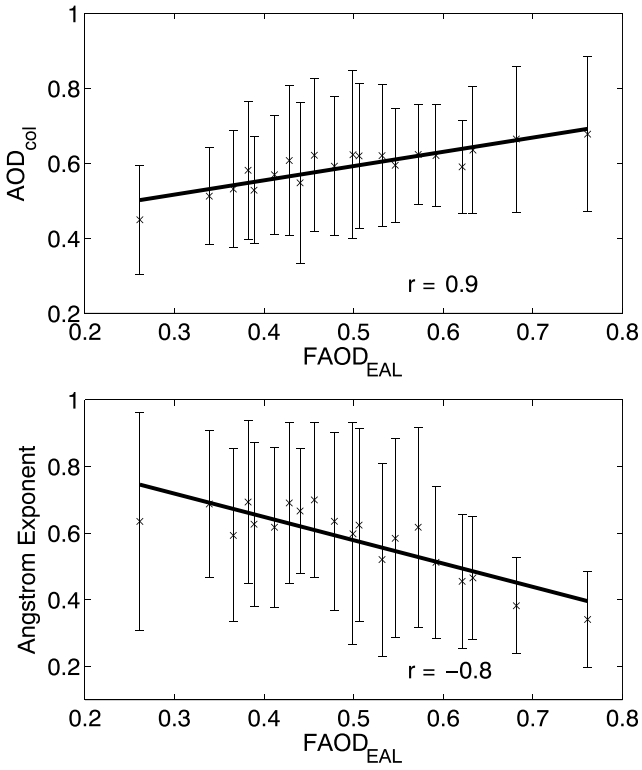

Figure 2. Association of (top) columnar AOD and (bottom) Angstrom exponent, both from AERONET measurements with fractional contribution to columnar AOD from EAL ($FAOD_{EAL}$) calculated from collocated MPLNET profiles. The sample set containing all collocated AERONET-MPLNET measurements during P9, P10, and P11 is divided into 21 bins of 5 percentile each. Legend shows the correlation coefficient (r) values significant at 99% confidence intervals.

21 bins of 5% each. Similar plots for each period are shown in Figure S2 in the supporting information. The crosses and vertical lines indicate mean and standard deviation for each bin, respectively. We find a significant (at 99% confidence interval) positive correlation coefficient ($r = 0.9$) between $FAOD_{EAL}$ and AOD_{col}. At the same time, we also find a significant (at 99% confidence interval) negative correlation coefficient ($r = -0.8$) between $FAOD_{EAL}$ and Angstrom exponent. The bin-averaged columnar Angstrom exponents are in the range of 0.4–0.7 (Figure 2, bottom). These results together indicate that increase in $FAOD_{EAL}$ over this region is strongly associated with increase in AOD_{col} and coarse particles. Previous studies have established dust as a prime aerosol species over the IGP during premonsoon, which mixes with the high concentration of black carbon (BC) emissions from urban regions [*Tripathi et al.*, 2005b; *Dey et al.*, 2008; *Gautam et al.*, 2011; *Srivastava et al.*, 2012]. *Singh et al.* [2004] showed that dust is the prime contributor to AOD over Kanpur during premonsoon. They revealed that the diurnal variation in Angtrom exponent and columnar AOD was inversely related. Using transport model, *Das et al.* [2013] have shown that dust is transported across the Indo-Gangetic Plains (IGP) at ~700–850 hPa altitude range and is accumulated over Himalayan slopes during March–May. In agreement, several studies on aerosol profiles over the Indian region during premonsoon have also reported the presence of nonspherical coarser particles at elevated layers [*Komppula et al.*, 2012; *Mishra et al.*, 2010; *Niranjan et al.*, 2007]. A recent study by *Chatterjee et al.* [2012] over Darjeeling in Eastern Himalayas has shown strong positive association between measured concentration of calcium mineral at surface and columnar AOD suggesting that dust loading during premonsoon season is linearly related to increase in columnar AOD. In this context, our results indicate that increase in $FAOD_{EAL}$ over Kanpur may be due to advection of coarse particles at higher altitudes, which in turn increases the columnar aerosol loading and decreases the Angstrom exponent over the region.

To estimate the origin of air masses reaching EAL altitudes at 1130 LT over Kanpur, 7 days back trajectories are computed using HYSPLIT model. Figure 3 shows the mean back trajectories for the days when MPLNET profiles are available during P9 (blue), P10 (black), and P11 (red) and corresponding altitudes of air masses at three altitudes (1.5 km (a and b) , 2.5 km (c and d), and 3.5 km (e and f) in Figure 3). The spread of wind direction is shown by the thin vertical lines. The mean AOD distribution (Figure 3) during April–June (2009–2011) is created by averaging gridded Level 3 aerosol product (0.5° × 0.5°) derived from MISR satellite [*Diner et al.*, 1998] and shown in the background. The 7 day back trajectories show that air masses reaching Kanpur at 3.5 km during all the three periods originated mainly from the layer, 3–6 km, over Middle East region (Box 3 in Figure 3e). However, the air masses reaching Kanpur at 2.5 km and 1.5 km during P9, P10, and P11 originated from different regions and also traversed at different mean altitudes. The air masses reaching Kanpur at 1.5 km and 2.5 km during P9 traversed the heavily polluted western IGP region of Pakistan and India (Box 1 in Figure 3a), while during P10, the air masses traversed Thar Desert and Arabian Sea region (Box 2 in Figure 3c). During P11 the mean air masses reaching Kanpur at 1.5 and 2.5 km traversed at higher altitudes compared to P9 and P10 and

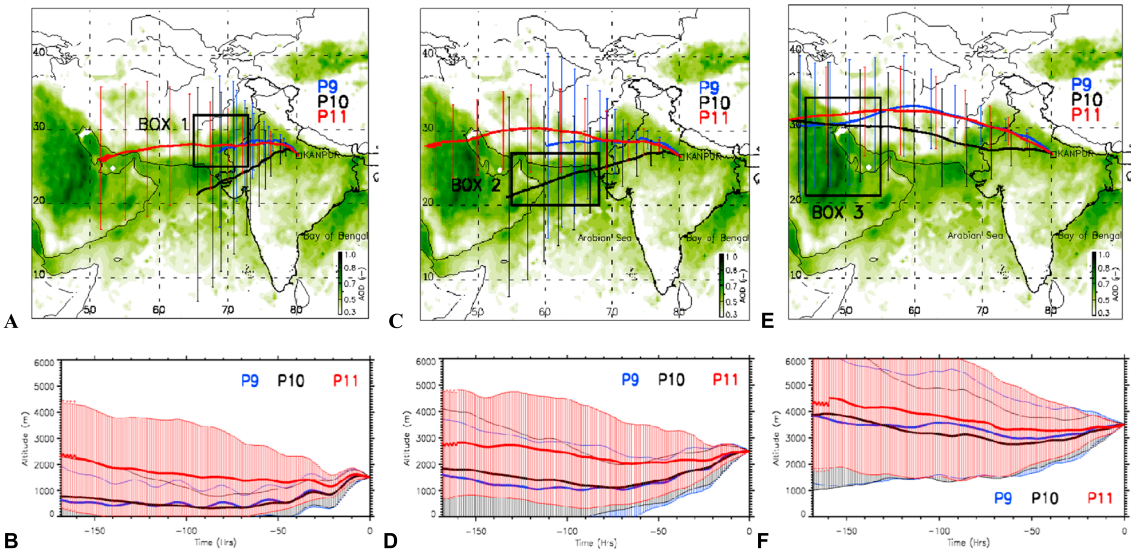

Figure 3. Back trajectories (7 day) and altitude variation for air masses reaching Kanpur (1130 LT) at (a, b) 1500 m, (c, d) 2500 m, and (e, f) 3500 m during periods P9 (blue), P10 (black), and P11 (red). The mean back trajectories in each period are average of days when MPLNET-observed σ profiles are available. The thin vertical lines across the mean back trajectories represent the spread of back trajectories in respective case. MISR-observed mean AOD (P9, P10, and P11) is illustrated in background of Figures 3a, 3c, and 3e. Black bounded Boxes 1–3 in Figures 3a, 3c, and 3e represent the source area for mean air masses reaching Kanpur below 3 km during P9, P10, and P11, respectively. The mean σ profiles over these boxes are shown in the supporting information (Figure S3).

were coming from as far as the Middle East. Mean AOD map shows high aerosol concentrations throughout the well-documented pathway (Saudi Arabia-Persian Gulf-Arabian Sea-Indus Valley in Pakistan-Thar Desert and northwestern IGP-Kanpur) of premonsoonal dust transport from Saudi Arabia to IGP [*Prasad et al.*, 2007; *Chinnam et al.*, 2006; *Liu et al.*, 2008; *Gautam et al.*, 2009; *Ram et al.*, 2010]. Moreover, the anthropogenic aerosols from the big urban agglomerates in Indus Valley and northwest IGP also get convected to midtroposphere and then advected to central IGP [*Kumar et al.*, 2015]. The air masses can bring aerosols with them to Kanpur from these heavily polluted/dusty regions (Boxes 1–3) lying in the trajectory paths of P9, P10, and P11. The aerosols present in EAL are mostly a mixture of coarse-sized natural and fine-sized anthropogenic aerosol (both transported and locally emitted). However, these back trajectories cannot help to make a sound conclusion about aerosol composition within EAL. A deep understanding of aerosol chemistry of EALs is essential, which warrants dedicated airborne experiments over this region in future.

The interannual differences in back trajectories at different altitudes may explain the observed interannual differences in aerosol vertical distribution over Kanpur (Figure 1). In order to explore the interannual variations in aerosol vertical extinction profiles, we investigated the CALIOP-derived aerosol vertical distribution at possible source regions (Boxes 1–3) for respective periods (Figure S3 in the supporting information). We consider Box 3 as source region for air masses reaching 3.5 km over Kanpur during P9, P10, and P11 (Figure S3a). The frequency distribution of aerosol extinction between 3 and 6 km altitude over Box 3 shows lower values during P11 compared to P9 and P10 (Figure S3b). Similarly, Boxes 1 and 2 are considered as the source regions for air masses reaching Kanpur at 1.5 and 2.5 km during P9, P10, and P11 (Figure S3c). The frequency distribution of σ between 1 and 3 km over these boxes shows that P11 exhibits higher frequency of large σ values (>0.15) (Figure S3d). These results suggest that higher aerosol concentration might be transported below 3 km during P11 compared to other periods. At the same time, the transported aerosol concentrations above 3 km are lower during P11 than that during P9 and P10. This analysis can explain the observed interannual differences in aerosol profiles. However, the local atmospheric structure could also modulate the aerosol profiles and can contribute to these interannual differences.

3.2. Daytime Variation of Aerosol Profiles

The mean daytime variation in aerosol vertical distribution (averaged for P9, P10, and P11) is shown in time-altitude plot by averaging the σ profiles every hour of the day from sunrise to sunset (Figure 4). Daytime variation in mixing layer height (black solid line) along with its standard deviation (dashed black line) is also shown in Figure 4. Increase in mixing height implies enhancement of turbulent mixing in the atmosphere. Aerosol vertical distributions show significant changes throughout the daytime. To highlight and quantify the

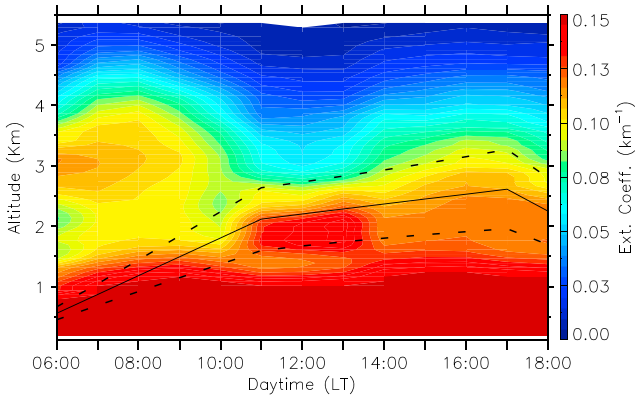

Figure 4. Time-altitude contour plot of mean vertical distribution (2009–2011, monsoon onset period) of σ averaged every hour of the day from sunrise to sunset. The black solid and dashed lines show mean mixing layer height and its variability, respectively.

daytime and interannual differences of the aerosol vertical distribution, especially EALs, during morning and evening period as compared to midday time, we grouped and averaged the σ profiles into three temporal bins: morning (0530 LT to 0930 LT, M), midday (0930 LT to 1530 LT, N), and evening (1530 LT to 1900 LT, E). Hereafter, we will refer M bin of P9 period as P9M and so on. It may be noted that the time intervals among the bins are different. This is done to reduce the difference in number of profiles available in each temporal bin. Figure 5 shows the mean σ profile for M (black), N (pink), and E (blue) time bins during P9 (top), P10 (middle), and P11 (bottom). The horizontal lines denote the standard deviation. The red lines in Figure 5 are the same exponential fitted curves used in Figure 1. The total number of profiles, scale height (h_{SL}), E(Surf), EAL_{crt}, AOD_{SL}, AOD_{EAL}, and $FAOD_{EAL}$ for each temporal bin are given in Table 1.

An elevated aerosol layer disconnected from the surface layer is present between 2 km and 4 km during morning period (0530 LT to 0930 LT) (Figure 4). The distinct EALs seen during morning period got dissipated with deepening of PBL by forenoon. As the PBL stabilizes in afternoon and starts subsiding by late evening, the distinct EALs are observed again. Figure 5 shows that the basic two-layered aerosol structure and the daytime variations in EALs from morning to evening are seen in all the three years. During morning and evening the EALs are parabolic shaped, while uniformly mixed EALs are observed during midday (Figure 5). The mean values of AOD_{EAL} are high during morning periods and decreases as the day progresses (Table 1). The decrease in AOD_{EAL} from morning to midday (evening) is 0.07 (0.09), 0.16 (0.12), and 0.03 (0.04) during P9, P10, and P11, respectively. The interannual variations in magnitude of AOD_{EAL} in each temporal bin (M, N, and E) are similar to that seen in Figure 1. We find that AOD_{EAL} was higher during P10M (0.44) and P9M (0.43) than that during P11M (0.33). EAL_{crt} also followed similar trend suggesting that EALs reached higher altitude during P10M (4.6 km) and P9M (3.9 km) as compared to that during P11M (3.3 km). In general, a uniformly mixed aerosol layer is found from 1.5 km to 4 km altitude during P9N and P10N but during P11N the mixed layer was below 3 km (Figure 5).

Aerosols which remain in the layer between stable nocturnal surface layer and entrainment zone after sunset are called the residual layer [*Stull*, 1988]. The distinct EALs observed during early morning periods might be the remnant of these residual layers from previous nights. However, EALs during morning periods are present at higher altitudes as compared to the EALs during evening periods. This may be due to the effect of some intense dust storm on certain days within the study period. To explore this, we have further analyzed the time-altitude profiles for individual years during morning periods (Figure S4). Figure S4 shows persistent high values of extinction between 3 and 5 km during P9 and P10, which is slightly decreased during P11 (2–4 km). The nighttime CALIPSO profiles (Figure S4) over Kanpur for three representative days (in P9, P10, and P11) show distinct elevated aerosol layer between 1.5 and 5 km. The interannual variation is also captured by these three representative profiles. These profiles suggest that the distinct morning EALs are a regular feature and may be the mixture of remnant aerosols from previous days and nighttime transported aerosol layers.

Mean AOD_{SL} is higher during midday as compared to morning and evening during all the three years (Table 1). The increase in AOD_{SL} from morning to midday is 0.05, 0.06, and 0.06 during P9, P10, and P11, respectively. Many previous studies over urban polluted cities have shown significant decrease in surface concentration of pollutants (especially BC) from morning to noon period due to enhanced dilution effect of increased boundary layer height during noon period (like *Ganguly et al.* [2006] for Delhi, *Safai et al.* [2007] for pune, and *Beegum et al.* [2009] for many sites over India). However, increase in AOD_{SL} as the day progresses from morning to afternoon indicates the dominance of increased surface emissions over the convective dilution effect (due to higher mixing height) in afternoon over Kanpur. This expected daytime variation can be explained as traffic

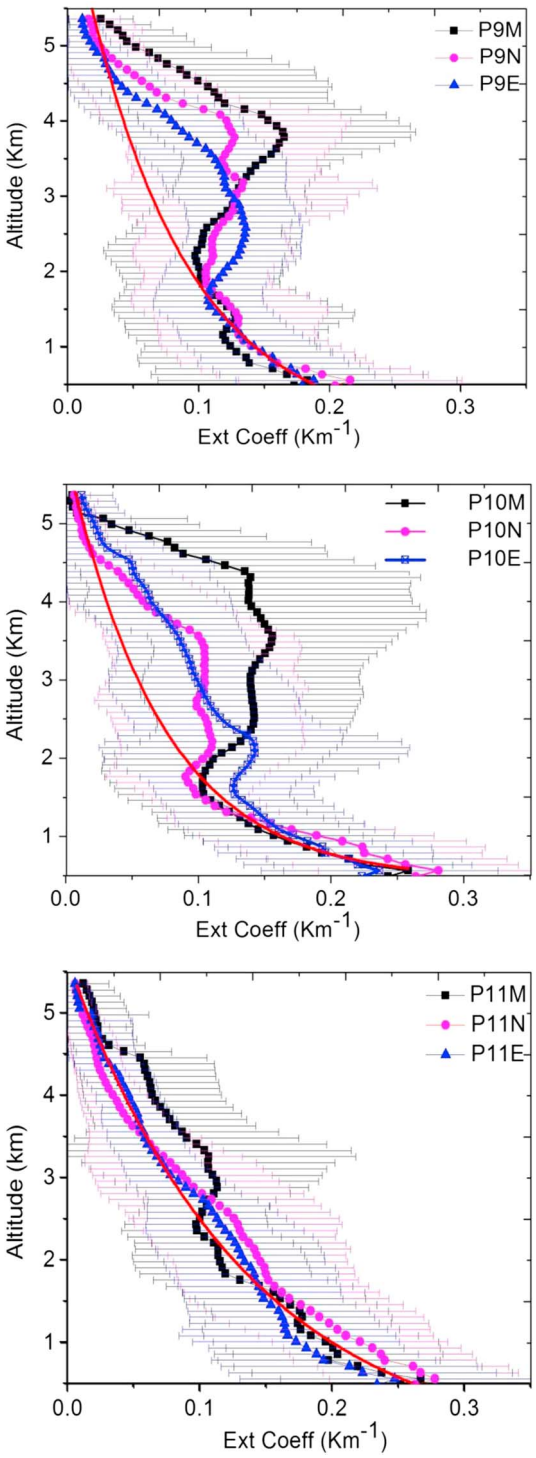

Figure 5. Mean σ profiles during (top) P9, (middle) P10, and (bottom) P11 segregated into three temporal bins, M (black), N (pink), and E (blue). The red line represents the exponential fit (equation 1) to the mean σ from 0.5 km to 1.5 km. Horizontal lines depict standard deviation.

and anthropogenic activities remain high between 0830 LT and 1630 LT over the IITK site [*Singh et al.*, 2004]. *Bisht et al.* [2015] also found midday increase in surface particulate matter concentration below 2.5 μm ($PM_{2.5}$) over Delhi during premonsoon season (contrary to winter and postmonsoon season), which is explained as increased contribution of resuspended dust particles during midday rush period. *Zhang et al.* [2012] studied the diurnal variations in aerosol concentration within aerosol boundary layer over Beijing and found noon period to be more polluted compared to morning period. The impact of frequent dust storms on the mean diurnal pattern of EAL and SL could be significant over this region during the monsoon onset period. Depending on the time of arrival of these dust storms at Kanpur, the mean diurnal pattern of aerosol profiles influenced by boundary layer dynamics and local emissions could get completely overshadowed [*Dey et al.*, 2004].

The dissipation of EALs from morning to midday with increase in mixing height can be attributed to a combination of vertical mixing with lower layers and horizontal advection of aerosol from our site to southern slopes of Indian Himalayas. *Dumka et al.* [2015] have shown that the concentration of surface pollutants over Nainital (in central Indian Himalayas) increased during midday with deepening of mixing height over IGP. They attributed this increase to contributions from transported aerosol mass from IGP region. Another study revealed that transported BC concentration from IGP contributes about 27% to observed surface BC concentration over Darjeeling in eastern Indian Himalayas [*Sarkar et al.*, 2015]. Increase in surface aerosol mass concentration during afternoon has also been found at Nepal Himalayan region [*Marinoni et al.*, 2010]. A recent study of CALIPSO-derived aerosol profiles has shown enhanced aerosol layer of nonspherical particles at high altitudes (between 15 and 18 km altitude), mainly due to deep convection during summer period over IGP [*Srivastava et al.*, 2016]. Using CAIPEEX measurements, *Prabha et al.* [2012] showed the removal of pollution from the IGP to higher atmospheric levels via dynamically forced updrafts. As premonsoon season is associated with deep convective activities over this region during midday [*Mishra and Shibata*, 2012], it may be also possible that aerosols are getting convected to higher altitudes (above 6 km) and are not captured by ground-based Level 2 MPLNET measurements due to low signal-to-noise ratio. Recently, a study over Beijing also showed that the upper boundary of elevated aerosols was greater during morning as compared to afternoon [*Zhang et al.*, 2012]. They have attributed this variation

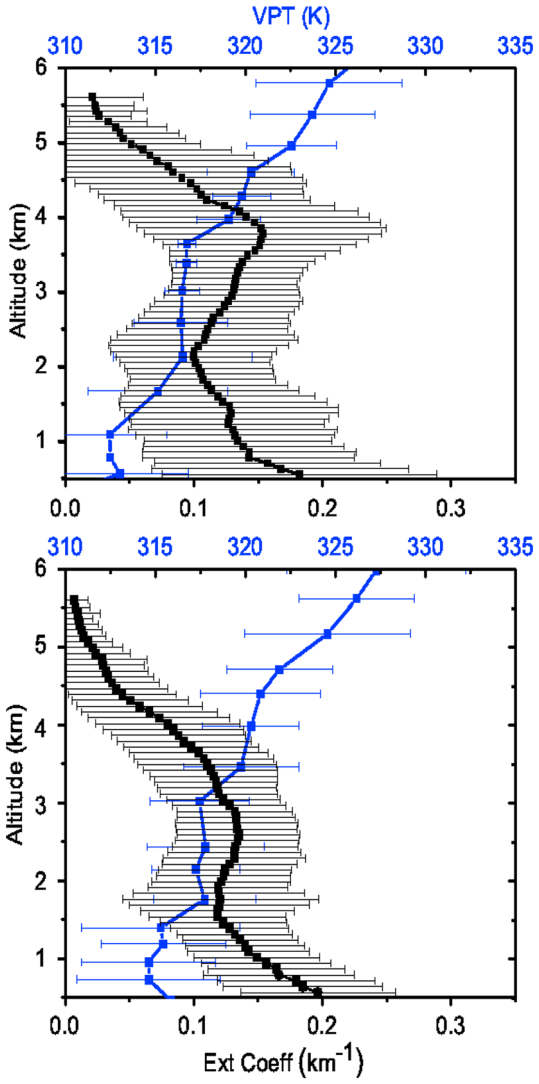

Figure 6. Mean σ profiles (black) with corresponding mean VPT profiles (blue) during (top) P9M and (bottom) P9E. Horizontal lines represent standard deviation.

to increase in aerosol boundary layer height and associated mixing from morning to afternoon. Aerosols emitted at the surface during midday could get convected to higher altitudes by late evening, which may explain the observed increase in $FAOD_{EAL}$ from midday to evening in all the three years (Table 1).

3.3. Aerosol Vertical Distribution and Meteorology: A Case Study

Several studies suggest that atmospheric stability and structure modulate the aerosol vertical distribution [*Raj et al.*, 2008; *Zhang et al.*, 2009]. *Mishra and Shibata* [2012] have suggested that the atmospheric instability over IGP during premonsoon season caused aerosol lofting to higher altitudes. EALs could be the result of either or both of the two sources: (1) aerosols advected by horizontal wind at high altitudes and/or (2) convected surface aerosols thermally capped at high altitudes. Correlation analysis between horizontal wind speed and σ is investigated to understand the difference in horizontal advection during P9M and P9E. We linearly interpolate σ to the same altitudes, wherever and whenever measurements of wind speed from radiosondes are available during P9M and P9E. We divide the region between altitude 0.5 km and 4.5 km into three bins: (a) 0.5 km to 1.5 km, (b) 1.5 km to 2.5 km, and (c) 2.5 km to 4.5 km. Statistically significant (>95% confidence interval) correlation coefficient (r) values are reported in Table S1.

The wind rose diagrams for air masses reaching Kanpur within these three layers are shown in Figure S5. It is found that most of the winds reaching Kanpur below 4.5 km are coming from the west and northwest direction (Figure S5) as also seen from our back trajectory analysis. The high correlation coefficients between σ and wind speed ($r \sim 0.6–0.8$) suggest that advected aerosols are present in considerable amount till 2.5 km altitudes, mainly coming from the west and northwest directions. No significant correlation is found in both cases (morning and evening) between 2.5 and 4.5 km. Daily mean Angstrom exponent-based segregation of the samples indicates that wind speed during dusty days (Angstrom exponent <0.6) may increase aerosol loading in this layer (2.5–4.5 km) but decrease during nondusty days (Angstrom exponent >0.6) resulting in an uncertain association (figure not shown). Also, during morning and evening, the upper part of this layer comprises interface between mixed layer and free troposphere (as discussed in the paragraph below), which may have more influence on the aerosol concentration in this layer compared to wind speed, thus resulting in uncertain correlation. Due to limitation of collocated and cotemporal data set, the sampling time of radiosonde measurements (0530 (1730)) and MPLNET profiles (0530–0930 (1630–1900)) during morning (evening) in this analysis is different. However, as the variation in aerosol profiles within M and E bin is less (Figure 4), we believe that the sampling difference could not affect significantly the quantitative nature of this analysis.

Capping inversion layer (CIL) is the interface of mixed layer (ML) and free troposphere (FT). Virtual potential temperature (VPT) profiles usually suffice for the identification of CIL. The sudden change in VPT gradient from nearly neutral to a persistent positive gradient identifies the beginning of CIL [*Stull*, 1988]. Figure 6 shows

the mean VPT profiles (blue) and mean σ profiles (black) during P9M (top) and P9E (bottom). A continuous statically stable atmosphere (FT) is present above 4.5 km during both the periods. A previous study [*Raman et al.*, 1990] also shows FT near 4.5 km during daytime over Delhi. The mean radiosonde profile in bin P9M shows that CIL is located between altitude 3.6 km and 4.5 km. EAL_{crt} is located (Table 1) near CIL during P9M and P9E. These associations suggest that the nearly neutral aerosol gradient in the lower portion of EAL was because of the turbulent mixing of aerosol in ML and the steep decreasing slope of aerosol distribution above EAL_{crt} was due to thermal capping of CIL. Similar association between temperature and aerosol profile was also reported by *Sinha et al.* [2013] on 16 April 2009 over Hyderabad. They found a well-mixed aerosol layer till 4 km below the CIL and steep decrease in aerosol concentration above 4.5 km.

3.4. Radiative Forcing Efficiency at Surface and TOA

The direct clear-sky shortwave (SW) aerosol radiative forcing (W m^{-2}) is defined as the difference between net SW fluxes (downward-upward) at a given atmospheric layer in aerosol-laden and aerosol-free conditions [*García et al.*, 2012; *McComiskey et al.*, 2008; *Christopher and Zhang*, 2002; *Boucher et al.*, 1998]; i.e., at surface (SRF), the direct SW aerosol radiative forcing is defined as

$$\Delta F^{SW}_{SRF} = \left(F^{a}_{\downarrow SRF} - F^{a}_{\uparrow SRF}\right) - \left(F^{0}_{\downarrow SRF} - F^{0}_{\uparrow SRF}\right) = \left(F^{a}_{\downarrow SRF} - F^{0}_{\downarrow SRF}\right) \times (1 - SA) \tag{5}$$

where $F^{a}_{\downarrow SRF}$ and $F^{a}_{\uparrow SRF}$ are downward and upward fluxes at surface in aerosol-laden conditions and $F^{0}_{\downarrow SRF}$ and $F^{0}_{\uparrow SRF}$ are downward and upward fluxes at surface in aerosol-free conditions. SA is surface albedo. Similarly, the SW aerosol radiative forcing at the TOA is defined as

$$F^{SW}_{TOA} = \left(F^{a}_{\downarrow TOA} - F^{a}_{\uparrow TOA}\right) - \left(F^{0}_{\downarrow TOA} - F^{0}_{\uparrow TOA}\right) = \left(F^{0}_{\uparrow TOA} - F^{a}_{\uparrow TOA}\right) \tag{6}$$

because at the TOA the downward flux is the same for either aerosol-free or aerosol-laden condition (i.e., $F^{a}_{\downarrow TOA} = F^{0}_{\downarrow TOA}$). The difference between the TOA and SRF radiative forcing is the atmospheric radiative forcing (ATM) that represents the energy trapped in the atmosphere due to the aerosol presence:

$$F^{SW}_{ATM} = F^{SW}_{TOA} - F^{SW}_{SRF} \tag{7}$$

Figure 7a shows the association between pyranometer-measured incoming total solar (TS) radiative fluxes at Earth's surface (TS_{SRF}) and temporally concurrent (within $\pm$5 min) AERONET-derived columnar AODs for P9 (blue), P10 (black), and P11 (red). The linear regression lines are also shown for respective years. Similarly, Figure 7b shows the linear regression between CERES-measured total shortwave solar outgoing flux at TOA (TS_{TOA}) with cotemporal MODIS-observed AOD over Kanpur. The correlation coefficients (r) significant at 99% confidence interval and the slope with uncertainty for both the regressions are mentioned in respective plot legends.

Aerosol SW radiative forcing efficiency (η in W m^{-2} AOD^{-1}) is the change in the SW aerosol radiative forcing per unit increase in AOD. The magnitude of slope of AOD flux regressions in Figures 7a and 7b provides the magnitude of radiative forcing efficiency, η, at SRF and TOA, respectively. However, it should be noted that the sign of radiative forcing efficiency at SRF would be the same as the sign of the slope in case of Figure 7a (equation (5)), whereas the same at TOA would be opposite to the sign of slope in case of Figure 7b (equation (6)). The difference between η at TOA and SRF will provide an estimate for radiative forcing efficiency in atmosphere.

The decrease in TS_{SRF} with increase in columnar AOD suggests aerosol-induced attenuation of incoming solar radiation at surface during all the three study periods (Figure 7a). The instantaneous forcing efficiencies (η) are -229.5 ± 26.8 W m^{-2} AOD^{-1} ($r = -0.8$), -179.5 ± 29.7 W m^{-2} AOD^{-1} ($r = -0.9$), and -255.1 ± 29.3 W m^{-2} AOD^{-1} ($r = -0.9$) during P9, P10, and P11, respectively. The interannual variability of η at surface may be attributed to the interannual difference in aerosol composition. The reported η of columnar aerosol loading on TS_{SRF} over Delhi (around 350 km from Kanpur) is -136.3 W m^{-2} AOD^{-1} during a dust-dominated period, April–June 2003 [*Singh et al.*, 2005], while *Gautam et al.* [2010] reported higher η values at surface (-188 W m^{-2} AOD^{-1}) over Kanpur during April–June of 2006–2007. *Li et al.* [2004] performed model calculations of SW surface η due to Saharan dust near the African coast. That study also illustrated that the value of η was higher (-81 W m^{-2} AOD^{-1}) for low dust season as compared to η (-65 W m^{-2} AOD^{-1}) for high dust season. *Pandithurai et al.* [2008] showed that modeled η values at surface over Delhi increased from

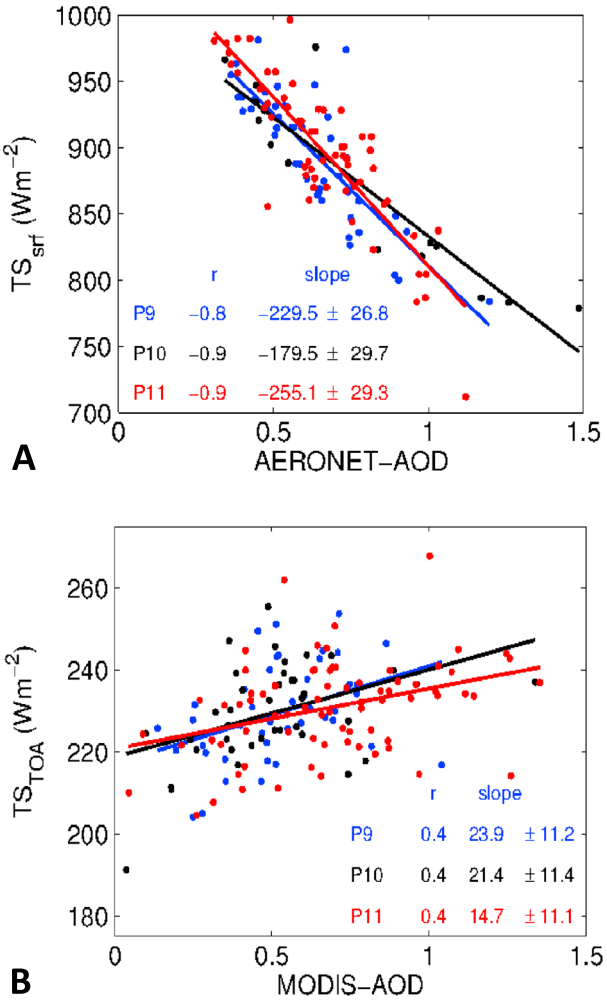

Figure 7. (a) Association between AERONET-observed AOD and pyranometer-measured incoming solar fluxes at surface (TS_{SRF}) over Kanpur for periods P9 (blue), P10 (black), and P11(red). (b) Similar association between MODIS-observed AOD and cotemporal CERES-measured outgoing shortwave fluxes at TOA (TS_{TOA}) over a 3° × 3° box centered over Kanpur. The legends show correlation coefficient (r) significant at 99% confidence interval and slope of regression with uncertainty. Although η at SRF will be the same as the slope in Figure 7a, η at TOA will be of opposite sign of the regression slope in Figure 7b. Please see equations (5) and (6) in text.

March (−71 W m^{-2}) to May (−87 W m−2) with increase in dust loading and thereby AOD values during 2006.

In contrast to TS_{SRF}-AOD association, TS_{TOA} shows a positive association with columnar AOD (Figure 7b). The increase in TS_{TOA} with increase in AOD suggests the increase in aerosol-induced backscattering of incoming solar radiation, i.e., cooling at TOA. The η values at TOA are -23.9 ± 11.2 W m^{-2} AOD^{-1} ($r = 0.4$), -21.4 ± 11.4 W m^{-2} AOD^{-1} ($r = 0.4$), and -14.7 ± 11.1 W m^{-2} AOD^{-1} ($r = 0.4$) during P9, P10, and P11, respectively. Our estimated η values at TOA are comparable with that of previous studies over this region. Using CERES-measured fluxes at TOA, *Rajeev and Ramanathan* [2001] showed that the magnitude of diurnal mean clear-sky outgoing solar radiation forcing efficiency at TOA was 24 W m^{-2} AOD^{-1} during March over northern India. We should note that the relatively weak association between outgoing SW flux at TOA and AOD (Figure 7b) could be a result of increased surface albedo over northern India (e.g., Kanpur) during the premonsoon season [*Gautam et al.*, 2010]. Therefore, the qualitative conclusion drawn from this analysis rather than quantitative values should be emphasized.

Simultaneous increase in TS_{TOA} and decrease in TS_{SRF} with AOD indicate the increase in both absorption and scattering of solar radiation by atmospheric aerosols. It should be noted that the association between AOD and radiation flux at surface (ground based) and TOA (satellite based) are analyzed from different platforms and have different spatial resolutions, which could affect the quantitative estimation of atmospheric aerosol forcing efficiency. Nonetheless, approximately threefold to fourfold lower aerosol forcing efficiencies at TOA as compared to that at surface and their differences (+195.6 W m^{-2} AOD^{-1} in P9, +158.1 W m^{-2} AOD^{-1} in P10, and +230.4 W m^{-2} AOD^{-1} in P11) imply significant warming of atmosphere per unit increase in AOD. An increase in AOD from 0.36 (25th percentile) to 0.67 (75th percentile) may absorb radiation of ~61 W m^{-2} causing atmospheric warming. Similarly for P10 and P11, a comparable increase in AOD (~0.3) may warm the atmosphere by 49 W m−2 and 71 W m^{-2}, respectively. The TOA and surface cooling along with atmospheric warming during premonsoon season was previously modeled over this region. Large positive shortwave atmospheric warming (37–75 W m−2) associated with negative surface and TOA cooling was found by *Kumar et al.* [2015] during dusty periods over Kanpur. The SW aerosol radiative forcing calculations performed over Delhi show large atmospheric warming (111–123 W m^{-2}) during May–June periods of 2006 [*Pandithurai et al.*, 2008]. *Jaidevi et al.* [2011] used in situ aircraft measured profiles at different places in central IGP during premonsoon period 2008. They reported diurnal averaged surface (atmospheric) forcing of −50 (+30) W m−2 (near Kanpur) and −80 (+53) W m^{-2} (near Bareilly, 200 km north of Kanpur).

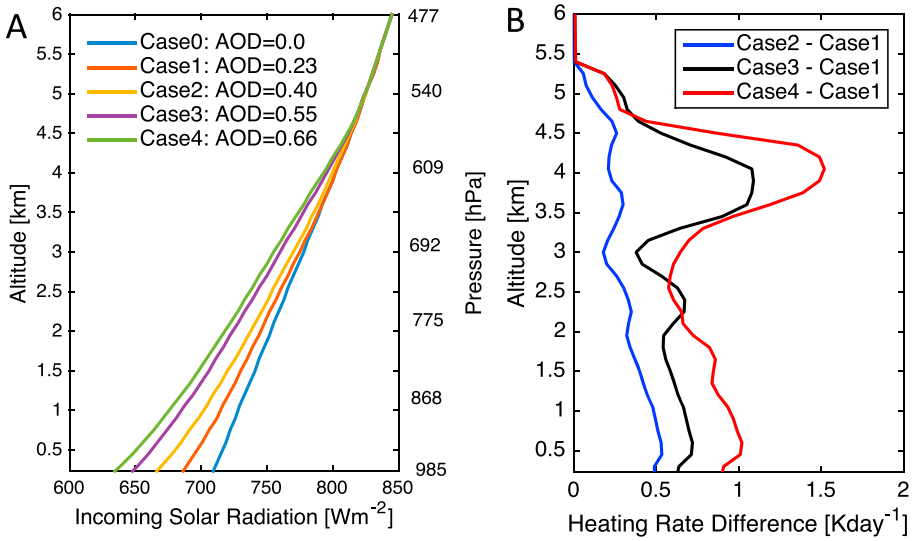

Figure 8. (a) Profiles of incoming SW radiation flux for five different SBDART simulations (in different colors). Legend shows the AOD values of each of the five simulations. (b) The difference in aerosol heating rate profiles between higher AOD cases and lowest AOD case. The aerosol heating rate is calculated as a difference between heating rate with and without aerosol (AOD = 0).

We have seen earlier (Figure 2) that the increase in AOD over Kanpur is associated with increase in fractional AOD of EAL ($FAOD_{EAL}$) and decrease in Angstrom exponent. Combination of these results (flux-AOD and $FAOD_{EAL}$-AOD association) indicates that EAL is an important factor, which may contribute to radiative changes at surface and TOA. We have used SBDART model to understand the importance of EAL in aerosol-radiation interaction using P10 as a case study. Figure S6 shows the inputs for SBDART simulations. Mean aerosol profiles as function of AOD are derived from MPLNET measurements by segregating all collocated AOD measurements into four equal bins (25% each). AODs mentioned in the legend are mean AODs of each bin. We have used AERONET-derived mean (P10) columnar single-scattering albedo (ω), asymmetry parameter (g), and Angstrom exponent (α) constant for all four AOD cases to explore the importance of EALs.

Figure 8a shows the profiles of incoming SW solar radiation fluxes (W m^{-2}) as a function of AOD. It shows a decrease in incoming SW solar radiation with increase in aerosol loading in lower troposphere (<4.0 km). This decrease is relatively higher below EAL (<1.5 km) with highest reduction near surface layer. As expected, there is no significant change in incoming radiation with AOD in layers (>5.0 km) above EALs. Aerosol heating rate profiles for each case are calculated as a difference between SBDART simulations with and without aerosols (AOD = 0). Figure 8b shows the differences in aerosol heating rate profiles between higher AOD cases and lowest AOD cases (as mentioned in the legend). We find that the increase in aerosol heating rate with increase in AOD is higher above ~3 km compared to that in lower layers (Figure 8b). Our results show maximum EAL heating rate to be ~1.5 K d^{-1} and ~0.5 K d^{-1} between 3 and 5 km altitudes for highest (mean AOD = 0.66) and lowest (mean AOD = 0.23) aerosol loading cases during P10. *Gautam et al.* [2010] found a peak value (~2 K d^{-1}) of aerosol heating rate at 3 km altitude over Kanpur during premonsoon of 2006–2007. A decadal study (2001–2010) over Kanpur revealed a mean heating rate of ~0.6–1.1 K d^{-1} between 1 and 4 km altitude during premonsoon, which increased to ~0.9–1.7 K d^{-1} during heavy aerosol loading cases [*Kaskaoutis et al.*, 2013]. *Dey and Tripathi* [2008] showed that mixed dust and black carbon could heat up the lower atmosphere up to 1 K d^{-1} during premonsoon of 2001–2005. A similar range (2.1–2.5 K d^{-1}) of heating rates in lower atmosphere (up to 5 km) were found over Delhi during May–June 2006 [*Pandithurai et al.*, 2008].

The increase in AOD (among the five cases used in our simulation) is associated with increase in $FAOD_{EAL}$ (Figure S6); therefore, the strong decrease in incoming radiation at lower tropospheric layers (Figure 8a) may be attributed to attenuation of a large fraction of incoming solar radiation by the elevated aerosols. In general, aerosols at higher altitudes would interact with more incoming radiation as compared to lower altitudes [*Mishra et al.*, 2015]. Therefore, relative increase in aerosol loading at EAL will cause strong attenuation of incoming solar radiation due to both aerosol-induced absorption and scattering of incoming radiation. The attenuation of radiation due to aerosols at an elevated layer can reduce the incident radiation to lower layers

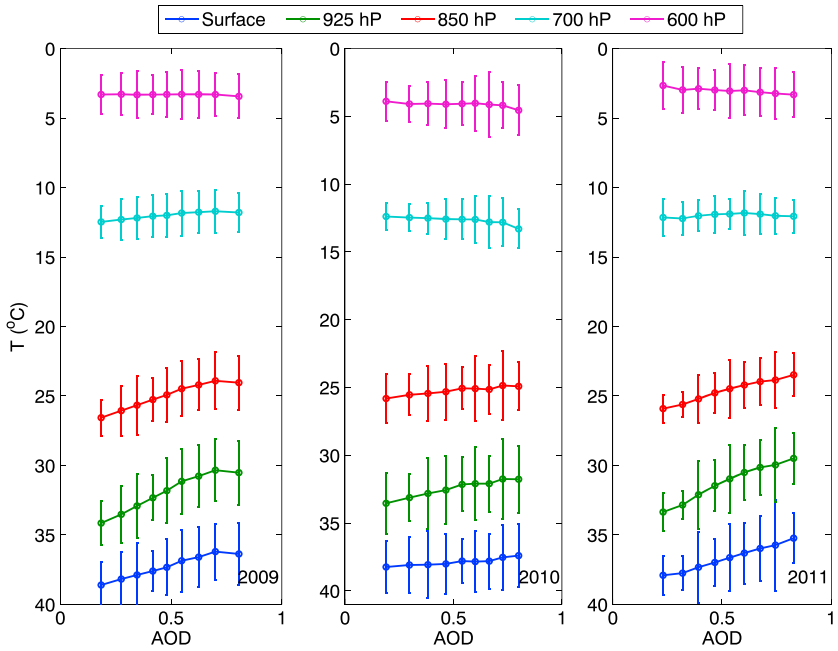

Figure 9. MODIS-AOD versus AIRS temperature at five different levels (Surface, 925, 850, 700, and 600 hPa) for P9, P10, and P11. The AIRS temperature data are sorted according to AOD and divided into nine bins of 10th percentile each between 5 and 95%. Error bars present the standard deviation of points in each bin. The mean altitudes representing the different pressure levels 925, 850, 700, and 600 hPa for each year are approximated using the radiosondes to be 0.7, 1.4, 3.1, and 4.5 km altitude, respectively.

as shown in Figure 8a. Although at this stage we cannot quantify the scattering effect of elevated aerosols, significant increase in aerosol heating rates of EALs suggests significant contribution of aerosol absorption in attenuation of incoming solar radiation by EALs.

3.5. Possible Implication of EAL-Radiation Interaction on Atmospheric Stability

How could the radiative effect of persistent EALs modulate the lower tropospheric stability during monsoon onset period over central IGP? To answer this question, we analyze collocated MODIS-observed AOD and AIRS-observed atmospheric temperature over a 3° × 3° area centered over Kanpur during all three periods. The temperature data are sorted according to AOD (only 5–95% of AOD data set is used) and divided into nine bins of 10th percentile each. The scatterplot of AOD and atmospheric temperature (at surface (2 m), 925, 850, 700, and 600 hPa pressure levels) is shown in Figure 9. The mean altitudes representing the different pressure levels 925, 850, 700 and 600 hPa are approximated using the radiosondes from Lucknow to be about 0.5, 1.3, 2.9, and 4.5 km, respectively.

Figure 9 shows a decrease in temperature with increase in AOD at surface (blue), 925 hPa (green), and 850 hPa (red) pressure levels. However, statistically insignificant changes (with respect to standard deviation) in atmospheric temperature are observed at 700 hPa (cyan) and 600 hPa (magenta). The standard deviation of temperature in each bin is the result of intraseasonal variation. The magnitude of cooling in the lower troposphere varies between 2 and 4°C during all the three periods. Temperature at 925 hpa (850 hpa) decreases by 3.6 (2.6), 1.8 (1.0), and 3.9 (2.4)°C as AOD increases from the lowest bin (mean AOD ~0.23) to the highest (mean AOD ~0.82) during P9, P10, and P11, respectively (Figure 9). The observed cooling with increase in AOD at surface is 2.2, 0.9, and 2.6°C during P9, P10, and P11, respectively. Although one will expect maximum cooling at surface with increase in AOD values, we find that the decrease in temperature within lower troposphere is highest at 925 hPa in all the three years. This could be explained as AIRS temperature retrievals are found to degrade near surface mainly due to the daytime convective buildup, heterogeneity of land surface properties and surface elevation (over land) [*Divakarla et al.*, 2006].

Sabbah [2010] found that the diurnal range of temperature in Kuwait reduced with heavy dust loading due to increase in atmospheric opacity. A recent study showed an overall lower tropospheric cooling up to $-0.7Kd^{-1}$ over Indian landmass for higher aerosol loading case as compared to lower aerosol loading using Weather

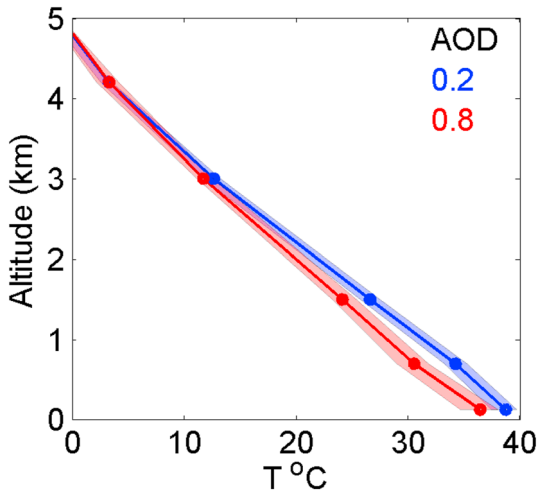

Figure 10. The comparison of atmospheric temperature profiles representing the lowest (blue) and highest (red) AOD bin (as shown in Figure 9). The solid lines represent the median atmospheric temperature profiles. The envelope represents the corresponding spread between 25% and 75%.

Research and Forecasting model coupled with Chemistry (WRF-Chem) for March 2012 [*Feng et al.*, 2016]. They explained the observed cooling as a dynamical response to both surface dimming and atmospheric heating by elevated aerosols. Aerosol-induced radiative effects reduced the temperature gradient between the land and atmosphere thereby decreasing the buoyancy of surface parcels. This leads to the reduction in boundary layer convection causing the lower tropospheric cooling [*Feng et al.*, 2016]. Large eddy simulations by *Barbaro et al.* [2013] also illustrated that elevated aerosol-induced surface dimming and stratification of lower troposphere can cause reduction in convective atmospheric boundary layer. Another WRF-Chem study showed a warming (0.8°C) effect at elevated layers and a cooling (−1.6°C) effect in lower layers due to increase in dust emission over the Indian region [*Dipu et al.*, 2013]. Similarly, in our study, higher aerosol absorption of incoming radiation at EALs as compared to lower tropospheric layers could affect the boundary layer dynamics and thereby result in lower tropospheric cooling. We find interannual differences in the rate of cooling between low and high aerosol bins. The cooling was lower during P10 as compared to P9 and P11, which is consistent with our SW aerosol radiative forcing analysis as η at surface during P10 was also minimum (Figure 7a). The interannual variations in aerosol-associated rate of cooling are mainly a result of differences in aerosol number concentration, aerosol chemical composition, and vertical structure. However, at this stage, we cannot rule out the possible large-scale meteorological impact on observed AOD-temperature association and its interannual variations. We did not find any significant warming at higher altitudes as shown by other studies [e.g., *Lau et al.*, 2006]. It could be possible that the temperature change below AIRS uncertainty range, i.e., 1 K [*Aumann et al.*, 2003], may not be captured by this analysis.

Further, we visualize the after effect of EAL-radiation association on atmospheric stability. Figure 10 illustrates the AIRS atmospheric temperature profiles (25th–75th percentiles) representing the lowest (blue, ~0.2) and highest AOD bin (red, ~0.8) using all the three periods together. The blue and red solid lines represent the median of the bins. The mean surface temperatures for low and high aerosol bin are 38.7 and 36.4°C, respectively. We find ~0.54°C/km decrease in environmental lapse rate from surface till 4 km between low AOD (lapse rate ~−8.85°C/km) and high AOD (lapse rate ~−8.31°C/km) scenario (Figure 10). These observations indicate increase in lower atmospheric stability for higher aerosol loading as compared to that for lower aerosol loading case. Thus, EALs may provide negative feedback to buoyancy of rising parcels from the surface. Although we have limited number of cotemporal radiosonde-temperature and MPLNET-aerosol profiles for P9E, similar analysis shows decrease in lower tropospheric temperature profile for high aerosol loading conditions (Figure S7a in the supporting information). Figure S7b shows corresponding mean aerosol profile for high and low aerosol loading cases. Combined feedback of reduction in surface fluxes and stabilization of boundary layer indicates that these EALs can affect cloud formation and precipitation patterns [*Dipu et al.*, 2013].

Modeling studies also suggest that these effects of aerosol over northern India can weaken the near-surface wind circulations, providing negative feedback to oncoming early phase monsoon [*Mahmood and Li*, 2013; *Collier and Zhang*, 2009]. However, several other studies [e.g., *Gautam et al.*, 2009; *Lau et al.*, 2006] reveal increase in early monsoonal rainfall over India due to midtropospheric warming caused by aerosol absorption. Moreover, the dynamical effect of dust radiative forcing may impart a positive feedback on the summer monsoon circulation over India [*Das et al.*, 2015; *Solmon et al.*, 2015]. Therefore, the aerosol-rainfall interaction over the region is a highly complicated issue and needs further detailed study using both observations and numerical models.

4. Summary

This study presents the interannual and daytime variation of aerosol vertical distribution and their radiative impacts over Kanpur, one of the largest industrial cities in IGP. Synergistic analyses of various satellites (MODIS, CERES, and AIRS) and ground-based remote sensors (MPLNET, AERONET, pyranometer, and radiosondes) are used during monsoon onset period (May–June) for three years (2009–2011). The salient features of this study are listed below:

1. Aerosol vertical σ profiles are measured from sunrise to sunset with high accuracy and frequency using MPLNET. We have observed two distinct aerosol layers: an exponentially decreasing surface layer (SL) below 1.5 km altitudes and an elevated aerosol layer (EAL), a region of accumulated lofted aerosols between 1.5 and 5.5 km altitudes. It is found that >50% of aerosols are generally lofted to elevated altitudes. The increase in fractional contribution of EALs is associated with transported coarse particles, which in turn also increases the total columnar AOD. EALs are a persistent phenomena during monsoon onset period of 2009–2011.
2. Substantial daytime variation exists in aerosol vertical distribution including shape, location, and optical thickness of EALs. Large distinct residual layers of elevated aerosol are observed during early morning period which disperse during midday with daytime evolution of boundary layer. Aerosols emitted into SL during midday are lofted to higher altitudes by evening. The distinct EALs again reappear by late evening.
3. Back trajectory analysis coupled with case studies of collocated radiosonde-measured variables suggests that transported aerosol from the Arabian Sea and Pakistan is reaching Kanpur, mainly below 2.5 km altitude. Interannual variability of aerosol profiles is associated with differences in transportation pathways and altitudes of air masses reaching Kanpur. However, interannual variation of local atmospheric structure can also modulate the aerosol vertical distribution. Thermal capping (inversion layer) near free troposphere may inhibit upward convection of aerosols across the entrainment zone and, thereby, could enhance the accumulation of aerosols below this inversion layer. The daytime variation in EALs is linked both with variations in local atmospheric structure as well as local emission and with vertical and horizontal transport of aerosols.
4. Collocated and cotemporal analysis of incoming shortwave solar flux with columnar AOD shows increase in surface cooling as a function of AOD during all the study periods. The SBDART analysis for 2010 shows that EALs have significant contribution in reduction of incoming surface flux in lower troposphere. This reduction was mainly the result of increase in absorbed radiation at EALs with increase in aerosol loading.
5. Collocated analyses of MODIS-AOD and AIRS-temperature show significant cooling of about 2–3°C in lower troposphere (>700 hPa) for high aerosol loadings. These radiative effects of EALs stabilize the lower troposphere, which could have impact on regional convection and large-scale atmospheric dynamics.

The differences in spatiotemporal resolution of various data (satellite- and ground-based sensors) used in this study could affect the quantitative analysis in view of daytime variation of measured optical quantities and their association with meteorological parameters. However, each separate analysis is performed using concurrent data sets to minimize the effect of sampling variations. Evaluation of aerosol vertical distribution and radiative impacts of EALs on the Indian summer monsoon using numerical models can be undertaken as follow-up studies. Our results can serve as a baseline for such studies, which can reduce uncertainty about aerosol direct radiative effect on monsoon dynamics.

Acknowledgments

The authors gratefully acknowledge the financial support given by the Earth System Science Organization, Ministry of Earth Sciences, Government of India (grant MM/NERC-MoES-03/2014/002) to conduct this research under Monsoon Mission. The authors would like to thank B.N. Holben and staff at NASA GSFC for establishing and processing data of the AERONET and SolRad-Net site at IIT Kanpur, used in this study. We acknowledge the use of radiosonde data freely available from University of Wyoming, the NCEP Reanalysis data provided by the NOAA/OAR/ESRL USA, and use of HYSPLIT model of NOAA-ARL for back trajectory analysis. MODIS, MISR, CERES,CALIPSO, and AIRS data sets were obtained from the NASA Langley Research Centre Atmospheric Science Data Center. All data measured at IITK are available on request from author (snt@iitk.ac.in). We also appreciate help from V.P. Kanawade in Figure 3.

References

Aumann, H. H., et al. (2003), AIRS/AMSU/HSB on the Aqua mission: Design, science objectives, data products, and processing systems, *IEEE Trans. Geosci. Remote Sens.*, *41*(2), 253–264.

Badarinath, K., S. K. Kharol, D. Kaskaoutis, A. R. Sharma, V. Ramaswamy, and H. Kambezidis (2010), Long-range transport of dust aerosols over the Arabian Sea and Indian region—A case study using satellite data and ground-based measurements, *Global Planet. Change*, *72*(3), 164–181, doi:10.1016/j.gloplacha.2010.02.003.

Barbaro, E., J. Vilà-Guerau de Arellano, M. C. Krol, and A. A. M. Holtslag (2013), Impacts of aerosol shortwave radiation absorption on the dynamics of an idealized convective atmospheric boundary layer, *Boundary Layer Meteorol.*, *148*, 31–49, doi:10.1007/s10546-013-9800-7.

Beegum, S. N., et al. (2009), Spatial distribution of aerosol black carbon over India during pre-monsoon season, *Atmos. Environ.*, *43*, 1071–1078, doi:10.1016/j.atmosenv.2008.11.042.

Bhattacharjee, P. S., A. K. Prasad, M. Kafatos, and R. P. Singh (2007), Influence of a dust storm on carbon monoxide and water vapor over the Indo-Gangetic Plains, *J. Geophys. Res.*, *112*, D18203, doi:10.1029/2007JD008469.

Bisht, D., U. Dumka, D. Kaskaoutis, A. Pipal, A. Srivastava, V. Soni, S. Attri, M. Sateesh, and S. Tiwari (2015), Carbonaceous aerosols and pollutants over Delhi urban environment: Temporal evolution, source apportionment and radiative forcing, *Sci. Total Environ.*, *521–522*, 431–445, doi:10.1016/j.scitotenv.2015.03.083.

Bollasina, M., S. Nigam, and K.-M. Lau (2008), Absorbing aerosols and summer monsoon evolution over South Asia: An observational portrayal, *J. Clim.*, *21*, 3221, doi:10.1175/2007JCLI2094.1.

Bollasina, M. A., Y. Ming, and V. Ramaswamy (2011), Anthropogenic aerosols and the weakening of the South Asian summer monsoon, *Science*, *334*, 502–505, doi:10.1126/science.1204994.

Boucher, O., et al. (1998), Intercomparison of models representing direct shortwave radiative forcing by sulfate aerosols, *J. Geophys. Res.*, *103*(D14), 16,979–16,998, doi:10.1029/98JD00997.

Boucher, O., et al. (2013), Clouds and aerosols, in *Climate Change 2013: The Physical Science Basis. Contribution of Working Group I to the Fifth Assessment Report of the Intergovernmental Panel on Climate Change*, pp. 571–657, Cambridge Univ. Press, Cambridge, U. K.

Campbell, J. R., D. L. Hlavka, E. J. Welton, C. J. Flynn, D. D. Turner, J. D. Spinhirne, V. S. Scott, and I. H. Hwang (2002), Full-time, eye-safe cloud and aerosol lidar observation at atmospheric radiation measurement program sites: Instruments and data processing, *J. Atmos. Oceanic Technol.*, *19*, 431, doi:10.1175/1520-0426(2002)019<0431:FTESCA>2.0.CO;2.

Chatterjee, A., S. K. Ghosh, A. Adak, A. K. Singh, P. C. Devara, and S. Raha (2012), Effect of dust and anthropogenic aerosols on columnar aerosol optical properties over Darjeeling (2200 m asl), eastern Himalayas, India, *PloS one*, *7*(7), E40286.

Cherian, R., C. Venkataraman, J. Quaas, and S. Ramachandran (2013), GCM simulations of anthropogenic aerosol-induced changes in aerosol extinction, atmospheric heating and precipitation over India, *J. Geophys. Res. Atmos.*, *118*(7), 2938–2955, doi:10.1002/jgrd.50298.

Chinnam, N., S. Dey, S. N. Tripathi, and M. Sharma (2006), Dust events in Kanpur, northern India: Chemical evidence for source and implications to radiative forcing, *Geophys. Res. Lett.*, *33*, L08803, doi:10.1029/2005GL025278.

Christopher, S. A., and J. Zhang (2002), Shortwave aerosol radiative forcing from MODIS and CERES observations over the oceans, *Geophys. Res. Lett.*, *29*(18), 1859, doi:10.1029/2002GL014803.

Chung, C. E., and V. Ramanathan (2006), Weakening of North Indian SST Gradients and the monsoon rainfall in India and the Sahel, *J. Clim.*, *19*, 2036–2045, doi:10.1175/JCLI3820.1.

Collier, J. C., and G. J. Zhang (2009), Aerosol direct forcing of the summer Indian monsoon as simulated by the NCAR CAM3, *Clim. Dyn.*, *32*, 313–332, doi:10.1007/s00382-008-0464-9.

Conant, W. C. (2000), An observational approach for determining aerosol surface radiative forcing: Results from the first field phase of INDOEX, *J. Geophys. Res.*, *105*(D12), 15,347–15,360.

Das, S., S. Dey, S. K. Dash, and G. Basil (2013), Examining mineral dust transport over the Indian subcontinent using the regional climate model, RegCM4.1, *Atmos. Res.*, *134*, 64–76, doi:10.1016/j.atmosres.2013.07.019.

Das, S., S. Dey, and S. K. Dash (2015), Impacts of aerosols on dynamics of Indian summer monsoon using a regional climate model, *Clim. Dyn.*, *44*, 1685–1697, doi:10.1007/s00382-014-2284-4.

Davidi, A., I. Koren, and L. Remer (2009), Direct measurements of the effect of biomass burning over the Amazon on the atmospheric temperature profile, *Atmos. Chem. Phys.*, *9*(21), 8211–8221.

Dey, S., and L. Di Girolamo (2011), A decade of change in aerosol properties over the Indian subcontinent, *Geophys. Res. Lett.*, *38*, L14811, doi:10.1029/2011GL048153.

Dey, S., and S. N. Tripathi (2008), Aerosol direct radiative effects over Kanpur in the Indo-Gangetic basin, northern India: Long-term (2001–2005) observations and implications to regional climate, *J. Geophys. Res.*, *113*(D4), D04212, doi:10.1029/2007JD009029.

Dey, S., S. N. Tripathi, R. P. Singh, and B. N. Holben (2004), Influence of dust storms on the aerosol optical properties over the Indo-Gangetic basin, *J. Geophys. Res.*, *109*, D20211, doi:10.1029/2004JD004924.

Dey, S., S. N. Tripathi, and S. K. Mishra (2008), Probable mixing state of aerosols in the Indo-Gangetic Basin, northern India, *Geophys. Res. Lett.*, *35*, L03808, doi:10.1029/2007GL032622.

Diao, M., L. Jumbam, J. Sheffield, E. F. Wood, and M. A. Zondlo (2013), Validation of AIRS/AMSU—A water vapor and temperature data with in situ aircraft observations from the surface to UT/LS from 87° N–67°S, *J. Geophys. Res. Atmos.*, *118*(12), 6816–6836, doi:10.1002/jgrd.50483.

Diner, D. J., et al. (1998), Multi-angle Imaging SpectroRadiometer (MISR) instrument description and experiment overview, *IEEE Trans. Geosci. Remote Sens.*, *36*, 1072–1087, doi:10.1109/36.700992.

Dipu, S., T. V. Prabha, G. Pandithurai, J. Dudhia, G. Pfister, K. Rajesh, and B. N. Goswami (2013), Impact of elevated aerosol layer on the cloud macrophysical properties prior to monsoon onset, *Atmos. Environ.*, *70*, 454–467, doi:10.1016/j.atmosenv.2012.12.036.

Divakarla, M. G., C. D. Barnet, M. D. Goldberg, L. M. McMillin, E. Maddy, W. Wolf, L. Zhou, and X. Liu (2006), Validation of Atmospheric Infrared Sounder temperature and water vapor retrievals with matched radiosonde measurements and forecasts, *J. Geophys. Res.*, *111*(D9), D09S15, doi:10.1029/2005JD006116.

Draxler, R. R., and G. D. Hess (1997), Description of the HYSPLIT_4 modeling system, Tech. Rep., Air Resources Laboratory.

Dumka, U. C., D. G. Kaskaoutis, M. K. Srivastava, and P. C. S. Devara (2015), Scattering and absorption properties of near-surface aerosol over Gangetic Himalayan region: The role of boundary-layer dynamics and long-range transport, *Atmos. Chem. Phys.*, *15*(3), 1555–1572, doi:10.5194/acp-15-1555-2015.

Eck, T. F., B. N. Holben, J. S. Reid, O. Dubovik, A. Smirnov, N. T. O'Neill, I. Slutsker, and S. Kinne (1999), Wavelength dependence of the optical depth of biomass burning, urban, and desert dust aerosols, *J. Geophys. Res.*, *104*, 31,333–31,350, doi:10.1029/1999JD900923.

Feng, Y., V. R. Kotamarthi, R. Coulter, C. Zhao, and M. Cadeddu (2016), Radiative and thermodynamic responses to aerosol extinction profiles during the pre-monsoon month over South Asia, *Atmos. Chem. Phys.*, *16*(1), 247–264, doi:10.5194/acp-16-247-2016.

Gadhavi, H., and A. Jayaraman (2006), Airborne lidar study of the vertical distribution of aerosols over Hyderabad, an urban site in central India, and its implication for radiative forcing calculations, *Ann. Geophys.*, *24*, 2461–2470, doi:10.5194/angeo-24-2461-2006.

Ganguly, D., A. Jayaraman, and H. Gadhavi (2006), Physical and optical properties of aerosols over an urban location in western India: Seasonal variabilities, *J. Geophys. Res.*, *111*, D24206, doi:10.1029/2006JD007392.

García, O. E., J. P. Díaz, F. J. Expósito, A. M. Díaz, O. Dubovik, Y. Derimian, P. Dubuisson, and J.-C. Roger (2012), Shortwave radiative forcing and efficiency of key aerosol types using AERONET data, *Atmos. Chem. Phys.*, *12*(11), 5129–5145, doi:10.5194/acp-12-5129-2012.

Gautam, R., N. C. Hsu, K.-M. Lau, and M. Kafatos (2009), Aerosol and rainfall variability over the Indian monsoon region: Distributions, trends and coupling, *Ann. Geophys.*, *27*, 3691–3703, doi:10.5194/angeo-27-3691-2009.

Gautam, R., N. C. Hsu, and K.-M. Lau (2010), Premonsoon aerosol characterization and radiative effects over the Indo-Gangetic Plains: Implications for regional climate warming, *J. Geophys. Res.*, *115*, D17208, doi:10.1029/2010JD013819.

Gautam, R., et al. (2011), Accumulation of aerosols over the Indo-Gangetic plains and southern slopes of the Himalayas: Distribution, properties and radiative effects during the 2009 pre-monsoon season, *Atmos. Chem. Phys.*, *11*, 12,841–12,863, doi:10.5194/acp-11-12841-2011.

Gu, L., J. D. Fuentes, M. Garstang, J. T. da Silva, R. Heitz, J. Sigler, and H. H. Shugart (2001), Cloud modulation of surface solar irradiance at a pasture site in Southern Brazil, *Agric. For. Meteorol.*, *106*(2), 117–129, doi:10.1016/S0168-1923(00)00209-4.

Holben, B. N., et al. (1998), AERONET: A federated instrument network and data archive for aerosol characterization, *Remote Sens. Environ.*, *66*(D11), 1–16, doi:10.1016/S00344257(98)00031-5.

Jaidevi, J., S. N. Tripathi, T. Gupta, B. N. Singh, V. Gopalakrishnan, and S. Dey (2011), Observation-based 3-D view of aerosol radiative properties over Indian Continental Tropical Convergence Zone: Implications to regional climate, *Tellus, Ser. B*, *63*(5), 971–989, doi:10.1111/j.1600-0889.2011.00580.x.

Kaskaoutis, D. G., S. K. Kharol, P. R. Sinha, R. P. Singh, K. V. S. Badarinath, W. Mehdi, and M. Sharma (2011), Contrasting aerosol trends over South Asia during the last decade based on MODIS observations, *Atmos. Meas. Tech. Discuss.*, *4*, 5275–5323, doi:10.5194/amtd-4-5275-2011.

Kaskaoutis, D. G., R. P. Singh, R. Gautam, M. Sharma, P. G. Kosmopoulos, and S. N. Tripathi (2012), Variability and trends of aerosol properties over Kanpur, northern India using AERONET data (2001–2010), *Environ. Res. Lett.*, *7*(2), 24,003–24,011, doi:10.1088/1748-9326/7/2/024003.

Kaskaoutis, D. G., P. R. Sinha, V. Vinoj, P. G. Kosmopoulos, S. N. Tripathi, A. Misra, M. Sharma, and R. P. Singh (2013), Aerosol properties and radiative forcing over Kanpur during severe aerosol loading conditions, *Atmos. Environ.*, *79*, 7–19, doi:10.1016/j.atmosenv.2013.06.020.

Kaskaoutis, D. G., E. E. Houssos, D. Goto, A. Bartzokas, P. T. Nastos, P. R. Sinha, S. K. Kharol, P. G. Kosmopoulos, R. P. Singh, and T. Takemura (2014), Synoptic weather conditions and aerosol episodes over Indo-Gangetic Plains, India, *Clim. Dyn.*, *43*, 2313–2331, doi:10.1007/s00382-014-2055-2.

Kinne, S., and R. Pueschel (2001), Aerosol radiative forcing for Asian continental outflow, *Atmos. Environ.*, *35*(30), 5019–5028, doi:10.1016/S1352-2310(01)00329-6.

Komppula, M., et al. (2012), Technical note: One year of Raman-lidar measurements in Gual Pahari EUCAARI site close to New Delhi in India—Seasonal characteristics of the aerosol vertical structure, *Atmos. Chem. Phys.*, *12*(10), 4513–4524, doi:10.5194/acp-12-4513-2012.

Kuhlmann, J., and J. Quaas (2010), How can aerosols affect the Asian summer monsoon? Assessment during three consecutive pre-monsoon seasons from CALIPSO satellite data, *Atmos. Chem. Phys.*, *10*, 4673–4688.

Kulkarni, J., et al. (2012), The cloud aerosol interactions and precipitation enhancement experiment (CAIPEEX): Overview and preliminary results, *Curr. Sci*, *102*(3), 413–425.

Kumar, R., M. C. Barth, G. G. Pfister, V. S. Nair, S. D. Ghude, and N. Ojha (2015), What controls the seasonal cycle of black carbon aerosols in India?, *J. Geophys. Res. Atmos.*, *120*(15), 7788–7812, doi:10.1002/2015JD023298.

Kumar, S., S. Kumar, D. G. Kaskaoutis, R. P. Singh, R. K. Singh, A. K. Mishra, M. K. Srivastava, and A. K. Singh (2015), Meteorological, atmospheric and climatic perturbations during major dust storms over Indo-Gangetic Basin, *Aeolian Res.*, *17*, 15–31, doi:10.1016/j.aeolia.2015.01.006.

Lal, D. M., S. D. Ghude, S. D. Patil, S. H. Kulkarni, C. Jena, S. Tiwari, and M. K. Srivastava (2012), Tropospheric ozone and aerosol long-term trends over the Indo-Gangetic Plain (IGP), India, *Atmos. Res.*, *116*, 82–92, doi:10.1016/j.atmosres.2012.02.014.

Lau, K. M., M. K. Kim, and K. M. Kim (2006), Asian summer monsoon anomalies induced by aerosol direct forcing: The role of the Tibetan Plateau, *Clim. Dyn.*, *26*, 855–864, doi:10.1007/s00382-006-0114-z.

Li, F., A. M. Vogelmann, and V. Ramanathan (2004), Saharan dust aerosol radiative forcing measured from space, *J. Clim.*, *17*, 2558–2571, doi:10.1175/1520-0442(2004)017<2558:SDARFM>2.0.CO;2.

Liou, K.-N. (2002), *An Introduction to Atmospheric Radiation*, 2nd ed., pp. xiv+583, Academic Press, San Diego, Calif.

Liu, Z., et al. (2008), Airborne dust distributions over the Tibetan Plateau and surrounding areas derived from the first year of CALIPSO lidar observations, *Atmos. Chem. Phys.*, *8*, 5045–5060.

Loeb, N. G., and S. Kato (2002), Top-of-atmosphere direct radiative effect of aerosols over the tropical oceans from the clouds and the Earth's Radiant Energy System (CERES) satellite instrument, *J. Clim.*, *15*, 1474–1484, doi:10.1175/1520-0442(2002)015<1474:TOADRE>2.0.CO;2.

Long, C. N., and T. P. Ackerman (2000), Identification of clear skies from broadband pyranometer measurements and calculation of downwelling shortwave cloud effects, *J. Geophys. Res.*, *105*(D12), 15,609–15,626, doi:10.1029/2000JD900077.

Mahmood, R., and S. Li (2013), Delay in the onset of South Asian summer monsoon induced by local black carbon in an AGCM, *Theor. Appl. Climatol.*, *111*, 529–536, doi:10.1007/s00704-012-0681-3.

Marinoni, A., et al. (2010), Aerosol mass and black carbon concentrations, a two year record at NCO-P (5079 m, Southern Himalayas), *Atmos. Chem. Phys.*, *10*(17), 8551–8562, doi:10.5194/acp-10-8551-2010.

McComiskey, A., S. E. Schwartz, B. Schmid, H. Guan, E. R. Lewis, P. Ricchiazzi, and J. A. Ogren (2008), Direct aerosol forcing: Calculation from observables and sensitivities to inputs, *J. Geophys. Res.*, *113*, D09202, doi:10.1029/2007JD009170.

Mishra, A. K., and T. Shibata (2012), Climatological aspects of seasonal variation of aerosol vertical distribution over central Indo-Gangetic belt (IGB) inferred by the space-borne lidar CALIOP, *Atmos. Environ.*, *46*, 365–375, doi:10.1016/j.atmosenv.2011.09.052.

Mishra, A. K., K. Klingmueller, E. Fredj, J. Lelieveld, Y. Rudich, and I. Koren (2014), Radiative signature of absorbing aerosol over the eastern Mediterranean Basin, *Atmos. Chem. Phys.*, *14*(14), 7213–7231, doi:10.5194/acp-14-7213-2014.

Mishra, A. K., I. Koren, and Y. Rudich (2015), Effect of aerosol vertical distribution on aerosol-radiation interaction: A theoretical prospect, *Heliyon*, *1*(2), E00036, doi:10.1016/j.heliyon.2015.e00036.

Mishra, M. K., K. Rajeev, B. V. Thampi, K. Parameswaran, and A. K. M. Nair (2010), Micro pulse lidar observations of mineral dust layer in the lower troposphere over the southwest coast of Peninsular India during the Asian summer monsoon season, *J. Atmos. Sol. Terr. Phys.*, *72*, 1251–1259, doi:10.1016/j.jastp.2010.08.012.

Misra, A., S. N. Tripathi, D. S. Kaul, and E. J. Welton (2012), Study of MPLNET-derived aerosol climatology over Kanpur, India, and validation of CALIPSO level 2 version 3 backscatter and extinction products, *J. Atmos. Oceanic Technol.*, *29*(3), 1285–1294, doi:10.1175/JTECH-D-11-00162.1.

Niranjan, K., B. L. Madhavan, and V. Sreekanth (2007), Micro pulse lidar observation of high altitude aerosol layers at Visakhapatnam located on the east coast of India, *Geophys. Res. Lett.*, *34*(3), L03815, doi:10.1029/2006GL028199.

Ozkaynak, H., A. Schatz, and G. Thurston (1985), Relationships between aerosol extinction coefficients derived from airport visual range observations and alternative measures of airborne particle mass, *J. Air Pollut. Control Assoc.*, *35*(11), 1176–1185.

Pandithurai, G., S. Dipu, K. K. Dani, S. Tiwari, D. S. Bisht, P. C. S. Devara, and R. T. Pinker (2008), Aerosol radiative forcing during dust events over New Delhi, India, *J. Geophys. Res.*, *113*, D13209, doi:10.1029/2008JD009804.

Parrish, D. F., and J. C. Derber (1992), The National Meteorological Center's spectral statistical-interpolation analysis system, *Mon. Weather Rev.*, *120*, 1747–1763, doi:10.1175/1520-0493(1992)120<1747:TNMCSS>2.0.CO;2.

Platnick, S., M. D. King, S. A. Ackerman, W. P. Menzel, B. A. Baum, J. C. Riedi, and R. A. Frey (2003), The MODIS cloud products: Algorithms and examples from Terra, *IEEE Trans. Geosci. Remote Sens.*, *41*, 459–473, doi:10.1109/TGRS.2002.808301.

Prabha, T. V., A. Karipot, D. Axisa, B. P. Kumari, R. S. Maheskumar, M. Konwar, J. R. Kulkarni, and B. N. Goswami (2012), Scale interactions near the foothills of Himalayas during CAIPEEX, *J. Geophys. Res.*, *117*, D10203, doi:10.1029/2011JD016754.

Prasad, A. K., S. Singh, S. Chauhan, M. K. Srivastava, R. P. Singh, and R. Singh (2007), Aerosol radiative forcing over the Indo-Gangetic Plains during major dust storms, *Atmos. Environ.*, *41*(29), 6289–6301, doi:10.1016/j.atmosenv.2007.03.060.

Raj, P. E., S. K. Saha, S. M. Sonbawne, S. M. Deshpande, P. C. S. Devara, Y. J. Rao, K. K. Dani, and G. Pandithurai (2008), Lidar observation of aerosol stratification in the lower troposphere over Pune during pre-monsoon season of 2006, *J. Earth Syst. Sci.*, *117*, 293–302, doi:10.1007/s12040-008-0032-z.

Rajeev, K., and V. Ramanathan (2001), Direct observations of clear-sky aerosol radiative forcing from space during the Indian Ocean Experiment, *J. Geophys. Res.*, *106*, 17,221–17,235, doi:10.1029/2000JD900723.

Ram, K., M. M. Sarin, and S. N. Tripathi (2010), A 1 year record of carbonaceous aerosols from an urban site in the Indo-Gangetic Plain: Characterization, sources, and temporal variability, *J. Geophys. Res.*, *115*, D24313, doi:10.1029/2010JD014188.

Raman, S., B. Templeman, S. Templeman, T. Holt, A. Murthy, M. Singh, P. Agarwaal, S. Nigam, A. Prabhu, and S. Ameenullah (1990), Structure of the Indian southwesterly pre-monsoon and monsoon boundary layers: Observations and numerical simulation, *Atmos. Environ. Part A*, *24*(4), 723–734, doi:10.1016/0960-1686(90)90273-P.

Ramanathan, V., and G. Carmichael (2008), Global and regional climate changes due to black carbon, *Nat. Geosci.*, *1*(4), 221–227.

Ramanathan, V., P. Crutzen, J. Kiehl, and D. Rosenfeld (2001), Aerosols, climate, and the hydrological cycle, *Science*, *294*(5549), 2119–2124.

Ramanathan, V., C. Chung, D. Kim, T. Bettge, L. Buja, J. T. Kiehl, W. M. Washington, Q. Fu, D. R. Sikka, and M. Wild (2005), Atmospheric brown clouds: Impacts on South Asian climate and hydrological cycle, *Proc. Natl. Acad. Sci. U.S.A.*, *102*(15), 5326–5333, doi:10.1073/pnas.0500656102.

Remer, L. A., et al. (2005), The MODIS aerosol algorithm, products, and validation, *J. Atmos. Sci.*, *62*, 947–973, doi:10.1175/JAS3385.1.

Ricchiazzi, P., S. Yang, C. Gautier, and D. Sowle (1998), SBDART: A research and teaching software tool for plane-parallel radiative transfer in the Earth's atmosphere, *Bull. Am. Meteorol. Soc.*, *79*, 2101–2114, doi:10.1175/1520-0477(1998)079<2101:SARATS>2.0.CO;2.

RosáRio, N. E., M. A. Yamasoe, H. Brindley, T. F. Eck, and J. Schafer (2011), Downwelling solar irradiance in the biomass burning region of the southern Amazon: Dependence on aerosol intensive optical properties and role of water vapor, *J. Geophys. Res.*, *116*, D18304, doi:10.1029/2011JD015956.

Sabbah, I. (2010), Impact of aerosol on air temperature in Kuwait, *Atmos. Res.*, *97*(3), 303–314, doi:10.1016/j.atmosres.2010.04.002.

Safai, P., S. Kewat, P. Praveen, P. Rao, G. Momin, K. Ali, and P. Devara (2007), Seasonal variation of black carbon aerosols over a tropical urban city of Pune, India, *Atmos. Environ.*, *41*(13), 2699–2709, doi:10.1016/j.atmosenv.2006.11.044.

Sarkar, C., A. Chatterjee, A. K. Singh, S. K. Ghosh, and S. Raha (2015), Characterization of black carbon aerosols over Darjeeling—A high altitude Himalayan station in eastern India, *Aerosol Air Qual. Res.*, *15*, 465–478.

Satheesh, S. K., V. Vinoj, and K. K. Moorthy (2006), Vertical distribution of aerosols over an urban continental site in India inferred using a micro pulse lidar, *Geophys. Res. Lett.*,*33*, L20816, doi:10.1029/2006GL027729.

Schafer, J. S., B. N. Holben, T. F. Eck, M. A. Yamasoe, and P. Artaxo (2002), Atmospheric effects on insolation in the Brazilian Amazon: Observed modification of solar radiation by clouds and smoke and derived single scattering albedo of fire aerosols, *J. Geophys. Res.*, *107*(D20), 8074, doi:10.1029/2001JD000428.

Seidel, D. J., C. O. Ao, and K. Li (2010), Estimating climatological planetary boundary layer heights from radiosonde observations: Comparison of methods and uncertainty analysis, *J. Geophys. Res.*, *115*, D16113, doi:10.1029/2009JD013680.

Seinfeld, J. H., and S. N. Pandis (2006), Chemistry of the atmosphoric aqueous phase, in *Atmospheric Chemistry and Physics: From Air Pollution to Climate Change*, 2nd ed., pp. 761–822, John Wiley, Hoboken, N. J.

Sharma, D., D. Singh, and D. G. Kaskaoutis (2012), Impact of two intense dust storms on aerosol characteristics and radiative forcing over Patiala, Northwestern India, *Adv. Meteorol.*, *2012*, 13, doi:10.1155/2012/956814.

Singh, R., S. Dey, S. Tripathi, V. Tare, and B. Holben (2004), Variability of aerosol parameters over Kanpur, northern India, *J. Geophys. Res.*, *109*, D23206, doi:10.1029/2004JD004966.

Singh, S., S. Nath, R. Kohli, and R. Singh (2005), Aerosols over Delhi during pre-monsoon months: Characteristics and effects on surface radiation forcing, *Geophys. Res. Lett.*, *32*, L13808, doi:10.1029/2005GL023062.

Sinha, P. R., R. K. Manchanda, D. G. Kaskaoutis, Y. B. Kumar, and S. Sreenivasan (2013), Seasonal variation of surface and vertical profile of aerosol properties over a tropical urban station Hyderabad, India, *J. Geophys. Res. Atmos.*, *118*, 749–768, doi:10.1029/2012JD018039.

Solmon, F., V. S. Nair, and M. Mallet (2015), Increasing arabian dust activity and the indian summer monsoon, *Atmos. Chem. Phys.*, *15*(14), 8051–8064, doi:10.5194/acp-15-8051-2015.

Srivastava, A. K., S. N. Tripathi, S. Dey, V. P. Kanawade, and S. Tiwari (2012), Inferring aerosol types over the Indo-Gangetic Basin from ground based Sun photometer measurements, *Atmos. Res.*, *109*, 64–75, doi:10.1016/j.atmosres.2012.02.010.

Srivastava, A. K., A. Misra, V. P. Kanawade, and P. C. S. Devara (2016), Aerosol characteristics in the UTLS region: A satellite-based study over north India, *Atmos. Environ.*, *125*, 222–230, doi:10.1016/j.atmosenv.2015.11.022.

Srivastava, S., S. Lal, S. Venkataramani, S. Gupta, and Y. B. Acharya (2011), Vertical distribution of ozone in the lower troposphere over the Bay of Bengal and the Arabian Sea during ICARB-2006: Effects of continental outflow, *J. Geophys. Res. Atmos.*, *116*, D13301, doi:10.1029/2010JD015298.

Stamnes, K., S.-C. Tsay, K. Jayaweera, and W. Wiscombe (1988), Numerically stable algorithm for discrete-ordinate-method radiative transfer in multiple scattering and emitting layered media, *Appl. Opt.*, *27*, 2502–2509, doi:10.1364/AO.27.002502.

Stull, R. B. (1988), *An Introduction to Boundary Layer Meteorology*, Atmospheric Sciences Library, Kluwer, Dordrecht, Netherlands.

Tripathi, S. N., S. Dey, A. Chandel, S. Srivastava, R. P. Singh, and B. N. Holben (2005a), Comparison of MODIS and AERONET derived aerosol optical depth over the Ganga Basin, India, *Ann. Geophys.*, *23*, 1093–1101, doi:10.5194/angeo-23-1093-2005.

Tripathi, S. N., S. Dey, V. Tare, S. K. Satheesh, S. Lal, and S. Venkataramani (2005b), Enhanced layer of black carbon in a north Indian industrial city, *Geophys. Res. Lett.*, *32*, L12802, doi:10.1029/2005GL022564.

Welton, E. J., and J. R. Campbell (2002), Micropulse lidar signals: Uncertainty analysis, *J. Atmos. Oceanic Technol.*, *19*, 2089–2094, doi:10.1175/1520-0426(2002)019<2089:MLSUA>2.0.CO;2.

Welton, E. J., K. J. Voss, H. R. Gordon, H. Maring, A. Smirnov, B. Holben, B. Schmid, J. M. Livingston, P. B. Russell, P. A. Durkee, P. Formenti, and M. O. Andreae (2000), Ground-based lidar measurements of aerosols during ACE2: Instrument description, results, and comparisons with other ground-based and airborne measurements, *Tellus, Ser. B*, *52*, 636–651, doi:10.1034/j.1600-0889.2000.00025.x.

Wielicki, B. A., B. R. Barkstrom, E. F. Harrison, R. B. Lee, G. L. Smith III, and J. E. Cooper (1996), Clouds and the Earth's Radiant Energy System (CERES): An Earth observing system experiment, *Bull. Am. Meteorol. Soc.*, *77*, 853–868, doi:10.1175/1520-0477(1996)077<0853:CATERE>2.0.CO;2.

Winker, D. M., M. A. Vaughan, A. Omar, Y. Hu, K. A. Powell, Z. Liu, W. H. Hunt, and S. A. Young (2009), Overview of the CALIPSO mission and CALIOP data processing algorithms, *J. Atmos. Oceanic Technol.*, *26*(11), 2310–2323, doi:10.1175/2009JTECHA1281.1.

Winker, D. M., J. L. Tackett, B. J. Getzewich, Z. Liu, M. A. Vaughan, and R. R. Rogers (2013), The global 3-D distribution of tropospheric aerosols as characterized by CALIOP, *Atmos. Chem. Phys.*, *13*, 3345–3361, doi:10.5194/acp-13-3345-2013.

Young, S. A., and M. A. Vaughan (2009), The retrieval of profiles of particulate extinction from Cloud-Aerosol Lidar Infrared Pathfinder Satellite Observations (CALIPSO) data: Algorithm description, *J. Atmos. Oceanic Technol.*, *26*, 1105, doi:10.1175/2008JTECHA1221.1.

Zhang, J., Q. Zhang, C. Tang, and Y. Han (2012), Aerosol structure and vertical distribution in a multi-source dust region, *J. Environ. Sci.*, *24*(8), 1466–1475.

Zhang, Q., X. Ma, X. Tie, M. Huang, and C. Zhao (2009), Vertical distributions of aerosols under different weather conditions: Analysis of in-situ aircraft measurements in Beijing, China, *Atmos. Environ.*, *43*(34), 5526–5535, doi:10.1016/j.atmosenv.2009.05.037.